UNIVERSITY OF CALIFORNIA SAN DIEGO

Silica Hollow Particles as Theranostic Agents for Tumor Imaging and Therapy

A dissertation submitted in partial satisfaction of the requirements for the degree Doctor of Philosophy

in

Chemical Engineering

by

James Wang

Committee in charge:

Professor Andrew C. Kummel, Chair
Professor Jesse Jokerst
Professor Jan Talbot
Professor William C. Trogler
Professor Kesong Yang

2019

The Dissertation of James Wang is approved, and it is acceptable in quality and form for production on microfilm and electronically:

_____

_____

_____

_____

_____

Chair

University of California San Diego

2019

TABLE OF CONTENTS

LIST OF FIGURES AND TABLES

ACKNOWLEDGEMENTS

I would like to acknowledge Professor Andrew Kummel for his support as the chair of my committee and also his invaluable guidance throughout my PhD journey. I would also like to acknowledge Professor William Trogler for his insights and guidance in science that has been immensely critical throughout my studies.

Chapter 1, in full, is the material as it appears in Advanced Functional Materials in 2015. Liberman, A., James Wang, N. Lu, Robert D. Viveros, C. A. Allen, R. F. Mattrey, S. L. Blair, W. C. Trogler, M. J. Kim, and A. C. Kummel, 2015. The dissertation author was the co-primary investigator and author of this paper.

Chapter 2, in full, is the material as it appears in IEEE Transactions on Medical Imaging, 2017. Wang, James, Christopher V. Barback, Casey N. Ta, Joi Weeks, Natalie Gude, Robert F. Mattrey, Sarah L. Blair, William C. Trogler, Hotaik Lee, and Andrew C. Kummel, 2017. The dissertation author was the primary investigator and author of this paper.

Chapter 3 , in full, is the material as it may appear in Advanced Therapeutics, 2019. Wang, James, Ching-Hsin Huang, Oscar H. Echeagaray, Siamak Amirfakhri, Sarah L. Blair, William C. Trogler, Andrew C. Kummel, Clark C. Chen, 2019. The dissertation author was the primary investigator and author of this paper.

I would like to acknowledge my group members including Prof. Sarah Blair, Alexander Liberman, Robert Viveros, Casey Ta, Jian Yang, Natalie Mendez, Ching-Hsin Huang, Christopher Barback, Adrian Badaracco, Maggie Tsai, Prof. Clark Chen, groups in SDSU and University of Chicago for their valuable assistance and input.

I would like to acknowledge my parents and my sister for their continuous support and discussions that help stimulate new thoughts in research

VITA

2006 Bachelor of Science, University of Washington

2017 Master of Science, University of California San Diego

2019 Doctor of Philosophy, University of California San Diego

PUBLICATIONS

1. **J. Wang**, et al. “Nanoshell Enhanced Acoustic Adjuvants for Immunotherapy in Glioblastoma.” ***Advanced Therapeutics*** (2019 accepted)
2. **J. Wang**, et al. "Extended Lifetime Pulse Stimulated Tumor Detection Ultrasound Imaging" ***IEEE Transactions on Medical Imaging*** 37.1 (2017): 222-229
3. A. Liberman*, **J. Wang* (Co-First)**, et al. "Mechanically Tunable Hollow Silica Ultrathin Nanoshells for Ultrasound Contrast Agents." ***Advanced Functional Materials*** 25, no. 26 (2015): 4049-4057
4. Y. Xie, J. Wang, **J. Wang** et al. “Long-lived, Versatile Ultrasound/Photoacoustic Contrast Agents via Fluorophilic Nanoparticle Stabilization” ***Journal of Materials Chemistry B*** (2019, accepted)
5. C.H. Huang, **J. Wang**, et al. “Thickness and Sphericity Control of Hard Shells Through Iron Doping: Low Threshold Ultrasound Contrast Agents.” ***Advanced Functional Materials*** (2019, accepted)
6. C.H. Huang, N. Mendez, O.H. Echeagaray, J. Weeks, **J. Wang**, et al. “Conjugation of a Small Molecule TLR7 Agonist to Silica Nanoshells Enhances Adjuvant Activity” ***ACS AMI*** (2019, accepted)
7. G.J. Anthony, K. Bader, **J. Wang**, et al. "MRI-guided transurethral insonation of silica-shell phase-shift emulsions in the prostate with an advanced navigation platform." ***Medical physics*** 46.2 (2019): 774-788
8. Y. Xie, **J. Wang**, et al. "Perfluorocarbon-loaded polydopamine nanoparticles as ultrasound contrast agents." ***Nanoscale*** 10.26 (2018): 12813-12819

9. J. Yang, E. Ward, T.W. Sung, **J. Wang**, et al. "Silica Shells/Adhesive Composite Film for Color Doppler Ultrasound Guided Needle Placement." ***ACS Biomaterials Science & Engineering*** 3.8 (2017): 1780-1787
10. J. Yang, **J. Wang**, et al. "Ultrasound Responsive Macrophase-Segregated Microcomposite Films for in Vivo Biosensing." ***ACS applied materials & interfaces*** 9.2 (2017): 1719-1727
11. N. Mendez, A. Liberman, J.A. Corbeil, C.V. Barback, R.Viveros, **J. Wang**, et al. "Assessment of in vivo Systemic Toxicity and Biodistribution of Iron-doped Silica Nanoshells" ***Nanomedicine*** 13.3 (2017): 933-942
12. Y. Huang, **J. Wang**, et al. "Polymer-stabilized perfluorobutane nanodroplets for ultrasound imaging agents." ***Journal of the American Chemical Society*** 139.1 (2016): 15-18
13. E.P. Ward **J. Wang**, et al. "Utilization of iron (III)-doped nanoshells for in vivo marking of nonpalpable tumors using a VX2 rabbit model." ***The American Journal of Surgery*** 212.6 (2016): 1140-1146
14. Liberman, Alexander, Zhe Wu, Christopher V. Barback, Robert D. Viveros, **J. Wang**, et al. "Hollow iron-silica nanoshells for enhanced high intensity focused ultrasound." ***Journal of Surgical Research*** 190, no. 2 (2014): 391-398.

ABSTRACT OF THE DISSERATION

Silica Hollow Particles as Theranostic Agents for Tumor Imaging and Therapy

By

James Wang

Doctor of Philosophy in Chemical Engineering

University of California San Diego, 2019

Professor Andrew C. Kummel, Chair

Silica micro and nanomaterials have been widely used in the biomedical field due to its chemical stability and flexibility, biocompatibility and ease of functionalization. Herein, silica micro and nanoshells were synthesized as a multifunctional theranostic tool in cancer imaging and therapy. Templated sol-gel method was employed to synthesize monodispersed silica hollow shells with thickness tunable by modulating the composition of silica precursors and organically modified alkoxysilanes. When ultrathin silica shells were filled with perfluorocarbon, a decreased acoustic threshold was observed when compared to silica shells synthesized with pure tetramethyl orthosilicate as a precursor. Furthermore, an increased ultrasound signal lifetime was achieved when compared to commercial microbubble based ultrasound contrast agents. Ultrathin silica shells with liquid perfluoropentane filled core were shown to exhibit a bimodal acoustic excitation profile where low acoustic power resulted in bubble oscillation and high acoustic power promoted bubble cavitation. Liquid filled ultrathin silica shells were chemically

and physically stable, acting as a long-term ultrasound tumor marking agent when intravenously injected into mice that were subcutaneously grafted with tumor. When intratumorally injected into tumor, liquid filled silica shells act as effect acoustic enhancer for high intensity focused ultrasound ablation. The presence of silica stabilized liquid perfluorocarbon resulted in generation of ultrasound signal in the form of cavitation clouds and decreased ultrasound intensity to generate mechanical ablation of tumor tissue and promote release of tumor neo-antigens. With concomitant administration of checkpoint blockade immunotherapy, three quarters of mice grafted with glioblastoma were induced into remission along with acquired immunity. These mice were characterized by increased tumor-infiltrating lymphocytes and T-cell activation. Silica hollow particles have been demonstrated as a flexible theranostic platform that can be used with ultrasound imaging and tumor ablation. When combined with current immunotherapies, silica hollow particles provide a myriad of opportunities to enhance efficacy without increasing potential drug burden.

INTRODUCTION

Background

Silica has been an attractive material used in nanomedicine research for applications, such as drug delivery,(1-6) protein/enzyme delivery,(7-9) and biomedical imaging.(10-13) Studies of medical applications of silica nanoparticles have been aided by the numerous synthetic techniques available to form particles with diverse sizes and structures(14-17) and robust *in vivo* stability and minimal toxicity.(18, 19) Different materials, such as surfactants and organically modified silanes, have been incorporated into the synthesis of silica nanoparticles to control their structures or sizes. For example, surfactants such as cetyltrimethylammonium bromide (CTAB) or various polymers are used in order to generate mesoporous silica nanoparticles.(20, 21) In addition to tetraalkoxysilanes, various mono-, bi-, and tri- substituted alkoxysilanes have been co-condensed to form silica nanoparticles. Typically these substituted alkoxysilanes are used to functionalize silica nanoparticles;(5, 19, 22) however, they have also been used in particle synthesis.(23-26)

Other sol-gel compatible materials have also been co-condensed with tetraalkoxysilane. For example, Mitchell et al. added iron (III) ethoxide during the synthesis of silica nanoshells to generate shells that break down in the presence of iron (III) chelating proteins.(27) Martinez and coworkers co-condensed trimethyl borate with tetramethyl orthosilicate (TMOS) to prepare microshells, which were mechanically strengthened *by incorporating* boron into the silica network.(28) Several reports have specifically investigated the mechanical properties of nanoparticle formulations. Zhang et al. had previously synthesized silica nanoshells which were tested by atomic force microscopy (AFM); it was found that particles with shell thickness as thin as 15 nm had the same Young's modulus as bulk silica.(29) It was also observed that the minimum force necessary to cause deformation in the silica shells increased as a function of the shell thickness squared.

There are many applications of silica nanostructures, including ultrasound contrast agents. These agents are typically synthesized by encapsulating a perfluorocarbon gas within a lipid or polymeric shell to produce elastic microbubbles in the range 1-6 μm in diameter.(30) When insonated, these microbubbles oscillate to produce signals at harmonic frequencies and, at resonance, break into smaller bubbles and collapse producing a broadband signal.(31) Since tissues only reflect the primary insonating frequency, contrast specific imaging provides a microbubble only image, which displays the location of the contrast agent on the image. Recently there have been several examples of silica based nanoparticle formulations that can also be used for contrast-enhanced ultrasound. The greatest advantage in using silica nanoparticles as ultrasound contrast agents compared to traditional liposomal/polymeric imaging agents is their improved *in vivo* stabilities and long imaging lifetimes. For example, gas filled silica particles could be continuously imaged for 45 minutes.(32) Iron-silica nanoshells filled with perfluoropentane could be imaged intermittently over the course of 10 days in a tumor bearing mouse with color Doppler imaging after intratumoral delivery of nanoshells.(33)

Ultrasound imaging is widely used in clinical diagnostics due to its portability, safety, and low cost (34). Ultrasound contrast agents were initially developed to study cardiac function and abnormalities (35-40). Injections of saline solution containing indocyanine green were discovered to result in echo clouds under ultrasound imaging that produces contrast with blood flow signals, and allows measurement of cardiac function (35, 41, 42). The contrast echoes originated from the microbubbles present in the injected solutions (42). As a result, microbubble based ultrasound contrast agents have been studied to optimize ultrasound backscatter and enable the imaging of capillary networks (43). Current ultrasound contrast agents are largely based on low-solubility gases, such as perfluorocarbons (PFC) or sulfur hexafluoride gas microbubbles, encapsulated within a flexible liposomal shell made from a polymer or lipid. However, microbubble ultrasound contrast agents such as Definity® exhibit short *in vivo* imaging lifetimes due to their fragile lipid composition and gas diffusion (44). For example, pressure gradients aid PFC gas dissolution into the surrounding bloodstream and dissipate the microbubble. Smaller

microbubbles result in larger Laplace pressures that further accelerate PFC gas dissolution and cause bubble collapse (45, 46). Additionally, bubble contraction and expansion during ultrasound exposure mechanically weakens the encapsulating lipid shell, resulting in short circulation lifetimes (45, 47, 48).

Glioblastoma is the most common form of adult brain cancer and one of the most aggressive human cancers (49-51). The median survival of glioblastoma patients after aggressive surgical resection, chemotherapy, and radiation therapy remains approximately 14 months (49). While immunotherapy through checkpoint inhibition has demonstrated impressive clinical efficacy against a number of tumor types (52-57), its application has been ineffective against glioblastomas (58). The clinical trial Checkmate 143 exploring the efficacy of the anti-PD1 antibody in recurrent glioblastoma patients showed no therapeutic effect (59). Subsequent investigations suggest that glioblastoma harbor a "cold" microenvironment, deplete of substrate immune cells required for effective anti-PD1 therapy (60, 61).

With this understanding, significant interest has emerged to design therapeutic strategies that induce accumulation of requisite immune cells in the glioblastoma microenvironment, thereby transforming a "cold" to a "hot" immune microenvironment. It is hypothesized that modalities affording this transition would augment the therapeutic efficacy of immunotherapies such as checkpoint blockade through anti-PD1 antibodies. Multiple methods have been developed to supplement PD-1 blockade therapies and reach therapeutic efficacy, yet each have certain limitations. Stereotactic radiation combined with PD-1 blockade has been shown to increase the median survival in mice by roughly twofold in glioblastoma but without induced remission (49). When using nanoscale hafnium (Hf) metal-organic frameworks (nMOFs) as radiation sensitizers, radiotherapy combined with PD-1 blockade induced remission on CT26 colon tumors with a 100 – 150 mm^3 starting volume (62). Nevertheless, radiation therapy is limited by the maximum X-ray dose that does not cause significant injuries to adjacent tissues or organs (62, 63). Photodynamic therapies with nanomaterials have also been combined with PD-1 blockade as potential treatment methods in breast and colorectal cancer models (64-67). However,

photodynamic therapy depends on the penetration depth of infrared lasers which varies with tissue type (68). Additionally, radiation or photodynamic therapies carry the potential for ablating the required immune cell mediator or cross-linking antigens thereby diminishing their immunogenicity. For glioblastoma, an ideal adjuvant therapy to PD-1 blockade treatment should be safe and able to reach deeper tissue structures while participating in the cellular mechanics of immunity re-stimulation. In addition to unique drug and nanoparticle adjuvant combinations (52, 69, 70), one such modality is acoustic based methods such as high intensity focused ultrasound (HIFU) (71, 72). Focused ultrasound based therapies have been demonstrated as a safe, non-invasive therapy for tumors deep in the body (71, 72). Since ultrasound energy is only focused at the focal point, tissue structures in the beam path are not affected, which results in a non-invasive ablation method with high penetration depth. Unlike other types of ablation methods such as RF, microwave, and laser ablation, HIFU is the only method that is non-invasive (73). Currently already used in clinical practice, thermal based HIFU has been used to treat uterine fibroids as well as kidney and brain tumors (73). However, thermal based HIFU can result in thermal stress at tissue locations adjacent to the focal zone due to heat diffusion and lead to potential cellular apoptosis (74). In contrast, mechanical HIFU is used to generate non-thermal effects that result in lesions with sharp borders of less than 200 μm (73). Nevertheless, there are unique challenges associated with HIFU as an immune-adjuvant technology. Heat generation from thermal HIFU (73) may compromise immune cell functions (75, 76) or trigger denaturation of the proteins required for tumor antigen presentation (75, 76). This consideration is largely addressed by employing low-duty cycle mechanical HIFU, which minimizes heat generation. Low duty cycle HIFU induces subcellular fragmentation resulting in ablative wounds that acts as a reservoir with highly concentrated populations of infiltrating dendritic cells (73). Previous studies have shown that low-duty cycle mechanical HIFU is more effective in stimulating immunological responses in melanoma and colon adenocarcinoma models relative to thermal HIFU (75). While checkpoint blockade therapies have been extensively studied and utilized in several cancer types, widespread application is limited by dose-dependent adverse effects;

therefore, physical, non-drug adjuvants such as mechanical HIFU are an attractive method to enhance the efficacy of a check point inhibitor without increasing drug burden.

Motivation

While aggressive cancer types such as glioblastoma are known to over express PD-L1 ligands, PD-1/PD-L1 blockade clinical trials have not shown promising results in improving glioblastoma survival rate. It has been observed that the glioblastoma tumor microenvironment is a highly immune suppressed environment that is known as a "cold" tumor. Existing combination immunotherapies including chemoradiation, chemo with immunotherapy and radiation with immunotherapy have not directly addressed the key issue of a cold tumor despite it's significant role in immunotherapeutic pathways. Since HIFU has been previously shown to result in inflamed tumor where dendritic cell infiltration is elevated, it is therefore hypothesized that mechanical HIFU can be used to convert a "cold" tumor, such as that found in glioblastoma, into a "hot" tumor that is vulnerable to anti-PD-1 checkpoint blockade therapies. Furthermore, unlike small molecule immunomodulators that are commonly used as adjuvants, a "physical," non-drug adjuvant such as mechanical HIFU does not introduce drug burden in addition to that of anti-PD-1 blockade antibodies, which have been shown to induce adverse side affects. In contrast, optimized mechanical HIFU that disrupts a closed and immune suppressed tumor microenvironment may further decrease the required dose of anti-PD-1 blockade for effective anti tumor effects. Lastly, the lack of tumor specificity with acoustic ablation methods such as mechanical HIFU represents a highly generalizable platform which can be used in a wide range of sold tumor cancer types where a conversion from cold to hot tumor would result in enhanced response to checkpoint blockade therapies.

Objective

To develop an acoustic method that converts a cold tumor to hot tumor via non thermal, mechanical ablation, an enhancement agent such as silica hollow particles was developed to focus and localize mechanical HIFU energy spatially. The primary objective is to minimize thermal elevation during

HIFU ablation, in order to minimize protein and antigen denaturation. Proteins such as damage associated molecular patterns (DAMPs) and tumor neo-antigens that are released during ultrasonic ablation are crucial for dendritic cell recognition and subsequent T cell priming during concomitant PD-1 checkpoint blockade therapy. If these molecules are thermally denatured, it would hinder the T cell re-stimulation process during PD-1 immunotherapies. While mechanical HIFU results in the intact release of DAMPs and tumor neo-antigens due to the lack of thermal depositions, an acoustic pressure per pulse higher than thermal HIFU is present due to the decrease of duty cycle from 100% (thermal HIFU) to 2% (mechanical HIFU) with the same output settings. A secondary objective is to develop silica shells filled with perfluorocarbon liquid that enhances the acoustic pressure via bubble cavitation effect, allowing for the use of lower pressured, clinically safer mechanical HIFU ablation. Due to bubble cavitation, these silica shells serve as an additional imaging agent for real-time ultrasound guided ablation, which can be useful for treating tumors at difficult physiological locations. The shell enhanced mechanical HIFU ablation procedures were developed with the aim to complement existing checkpoint blockade therapies by convert an immune suppressed (cold) tumor into an immune active (hot) tumor.

Approaches

To develop a platform for ultrasound guided mechanical HIFU that complements immunotherapy, a 3-step approach is employed:

1. Material Development: Silica hollow shells are optimized for ultrasound imaging and HIFU ablation. Organically modified silica precursors consisting of functional R groups (phenyl and fluorinated phenyl, octane and fluoro-octyl) that do not participate in a sol-gel condensation reaction were included to create shells with different mechanical strengths. Transmission electron microscopy were used for basic material characterization. The hollow shells were imaged with ultrasound using contrast specific imaging and color Doppler imaging.
2. *In Vivo* Imaging: Silica hollow shells with strong ultrasound contrast signal were evaluated in mice grafted with a slow growing tumor on the flank. Hollow shells were filled with

perfluorocarbon liquid, conjugated with tumor specific targeting ligand and intravenously injected for tumor localization and ultrasound imaging. Biodistribution studies with radiolabeling were also performed to investigate the location of the hollow shells after IV injections.

3. *In Vivo* Therapy: Hollow shells filled with liquid perfluoropentane and the enhancement effects on high intensity focused ultrasound (HIFU) were studied. Both thermal and mechanical HIFU were evaluated in terms of temperature increase and tissue lesion size. Shells were directly injected into tumors for mechanical HIFU enhancement to convert cold tumors into hot tumors. Anti-PD-1 antibodies were also administered to stimulate immune memory against glioblastoma tumors. In vivo mice experiments were evaluated with tumor progression, immunohistochemistry, and flow cytometry.

CHAPTER 1. MECHANICALLY TUNABLE HOLLOW SILICA ULTRATHIN NANOSHELLS FOR ULTRASOUND CONTRAST AGENTS

Silica nanoparticle growth can be modeled using a LaMer model(77) in which at a critical free energy, nanoparticles of a critical radius begin to form, which depends on concentration of precursor and other parameters. For silica, nanoparticles may result from either continued growth of nuclei or by agglomeration of smaller nuclei. Caruso et al. demonstrated that silica nanoshells could be synthesized by adsorbing 25 nm silica nanoparticles onto positively charged polystyrene templates and calcining them to produce hollow silica nanoshells.(17) This demonstrates that silica nanoparticles can be constructed in a hierarchical fashion similar to various nanoflake-nanoparticle formulations. The term nanoflake has been used to describe nanomaterials that are 2D with diameters or cross sections ranging from 1 nm - 500 nm. Nanoflake thicknesses typically fall in the sub-20 nm range with Mazur and co workers reporting on silver nanoflakes as thin as 0.5 nm.(78) Nanoflakes have been synthesized from a wide variety of materials for a spectrum of applications, such as improving electronic properties of materials or modifying thermal properties.(79-81) For example, Cui et al. showed that 100-200 nm diameter ceria (CeO_2) nanoparticles synthesized for catalysis were actually composed of an aggregate of *10 nm by 20 nm* nanoflakes.(82) These results suggest it may be possible to synthesize silica nanoparticles composed of a hierarchical structure of nanoflakes.

Ultrasound imaging power is referred to as mechanical index (MI), which is proportional to the peak negative pressure divided by the square root of the imaging frequency. Since silica particles produced greater signal as the MI was increased, it was proposed that there must be subpopulations of particles with varying mechanical strengths that fracture to release the gas at different pressures.(32) As a result, it is necessary to synthesize nanoshells with a larger percentage of the subpopulations that are mechanically weaker so that the ensemble can be imaged at lower MI for longer times. This was achieved by modifying the nanoshell synthesis with organically modified trialkoxysilanes which

produced nanoshells composed of an assembly of ultrathin nanoflakes. The ultrathin nanoshells had significantly lower color Doppler imaging thresholds, greater imaging longevities, and greater contrast specific imaging performance derived from improved nanostructures compared to control nanoshells made with only TEOS and thus thicker shells.

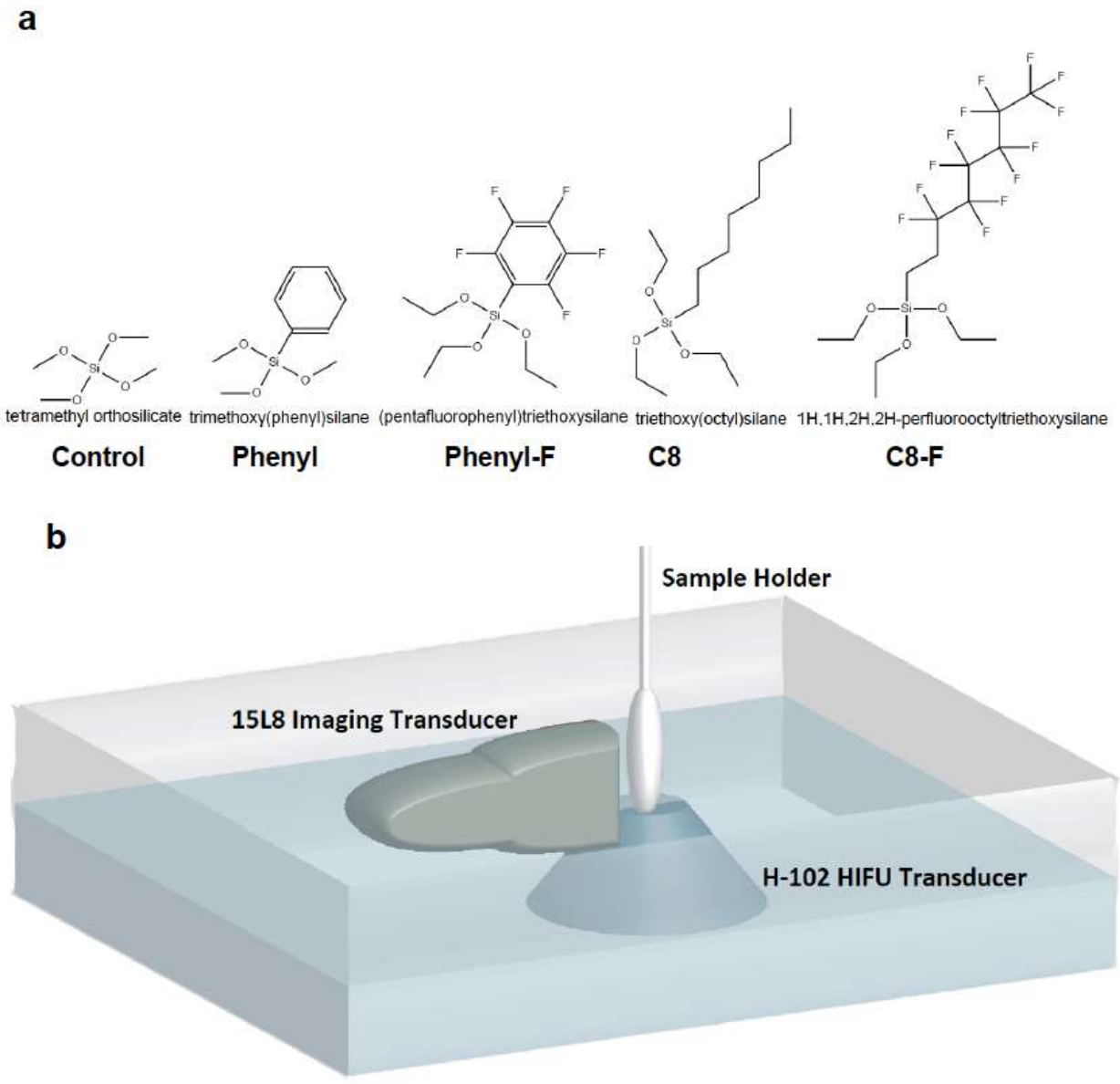

Figure 1.1 Structures of R-group substituted trialkoxysilanes and experimental set up for ultrasound testing of nanoshells.
A) Molecular structures and naming scheme of R-group substituted trialkoxysilanes used in the modified sol-gel synthesis. B) Experimental set up for ultrasound testing of nanoshells. Nanoshells were suspended in the sample holder at 400 μg/ml. The imaging transducer and the HIFU transducer were aligned orthogonally.

The structures of the organically modified trialkoxysilanes used in synthesis of the nanoshells can be viewed in Figure 1.1. SEM images show (Figure 1.2) that all formulations produce uniform 500 nm nanoshells; however, there are key structural differences between the advanced formulations compared with the **control** iron doped silica nanoshells which use 100% TMOS as the silica precursor (Figure 1.2A). (a) The surface morphology of the **C8** (Figure 1.2B) and **phenyl** (Figure 1.2D) particles are smoother compared to the other formulations. (b) For only the **C8** and **phenyl** formulations, the first layer of nanoshells is sufficiently transparent in SEM to observe the underlying 2nd layer of particles, which is consistent with thinner shell walls. The **control** nanoshells, **C8-F** nanoshells, and **phenyl-F** nanoshells have a layer of flaked silica on the outer surface of the nanoshell.

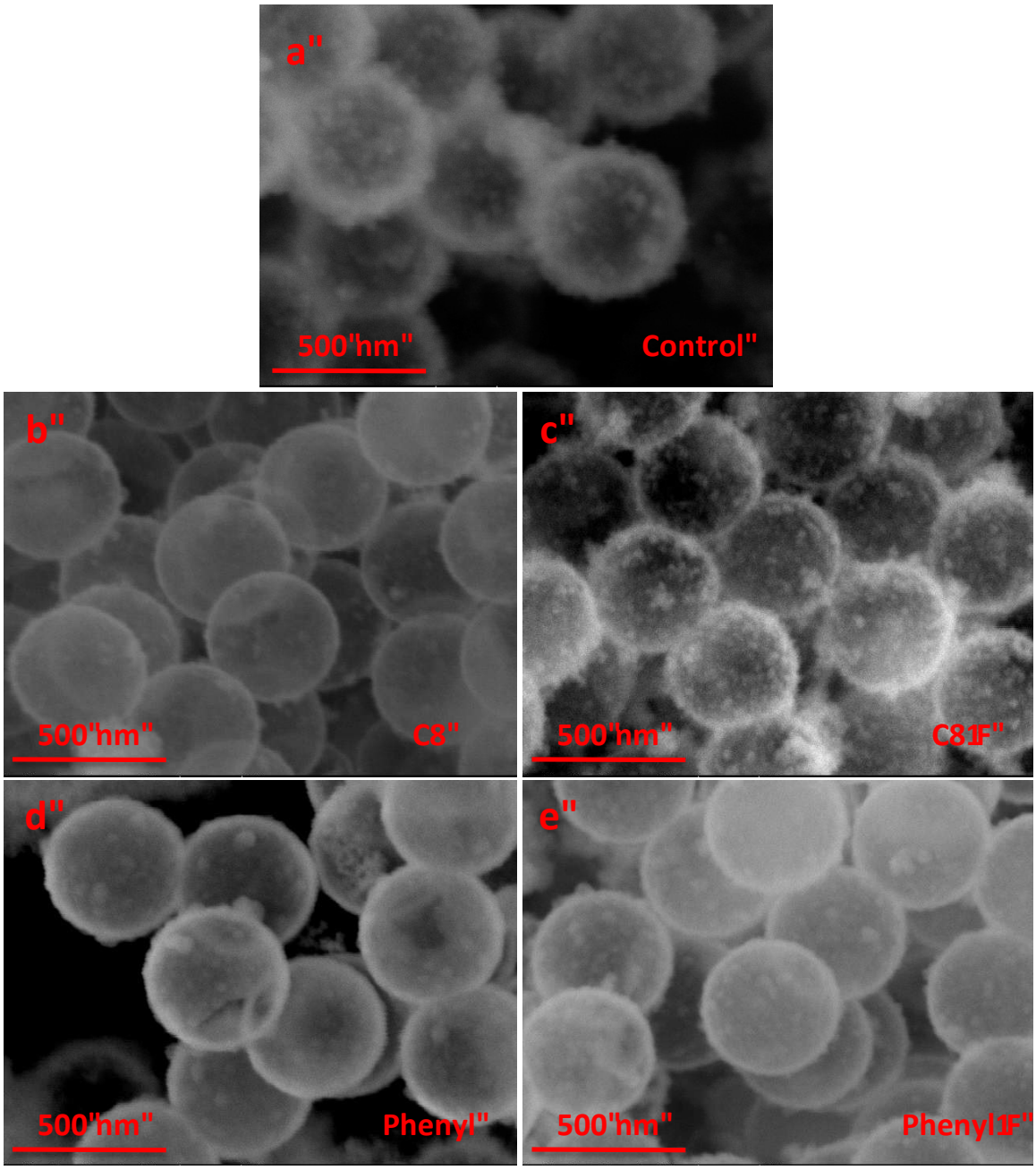

Figure 1.2 Scanning electron microscopy of various formulations.
74K Magnification was used after nanoshells have been calcined. A) **Control** nanoshells. B) Nanoshells synthesized with **C8** C) Nanoshells synthesized with **C8-F.** D) Nanoshells synthesized with **phenyl.** E) Nanoshells synthesized with **phenyl-F.** The transparent images of the **C8** and **phenyl** particles are consistent with the nanoflakes forming shells of a few nanometer thickness.

Iron-silica nanoshells were developed as an intraoperative color Doppler tumor marker, and nanoshells were characterized at 7 MHz, the previously determined optimal frequency, for color Doppler

imaging threshold and continuous imaging longevity *in vitro*.(28, 32, 33) As shown in Fig 1.3A, the **Phenyl**, **C8** and **C8-F** formulations had a lower MI threshold compared to the control particles. This is consistent with the particles being more sensitive to color Doppler imaging and consistent with the thinner shells observed for these formulations in SEM. The mechanism for color Doppler imaging of the rigid nanoshells has been shown to arise from nanoparticle fracture and release of entrapped perfluorocarbon gas.(28, 32) To measure the continuous imaging lifetime (Figure 1.3B), particles were imaged continuously at MI 1.9 until no signal could be generated from the sample. For the **phenyl** and the **C8** particles, signal continued to be readily observed at 180 min (Figure 1.3C-D). Since the same mass of particle was tested for all formulations, the differences in intensities and imaging lifetimes suggests that they arise from the differences in subpopulations of particles being imaged. It is hypothesized that for the **control**, **phenyl-F** and **C8-F** particles, large fractions of particles are too mechanically robust to be shattered during insonation and as such do not generate any ultrasound contrast signal. It is hypothesized that a greater fraction of **phenyl** and the **C8** particles are weakened as a result of thinner shells and thus have more ultrasound active particles per unit mass. A larger number of ultrasound sensitive particles results in a much longer imaging lifetime.

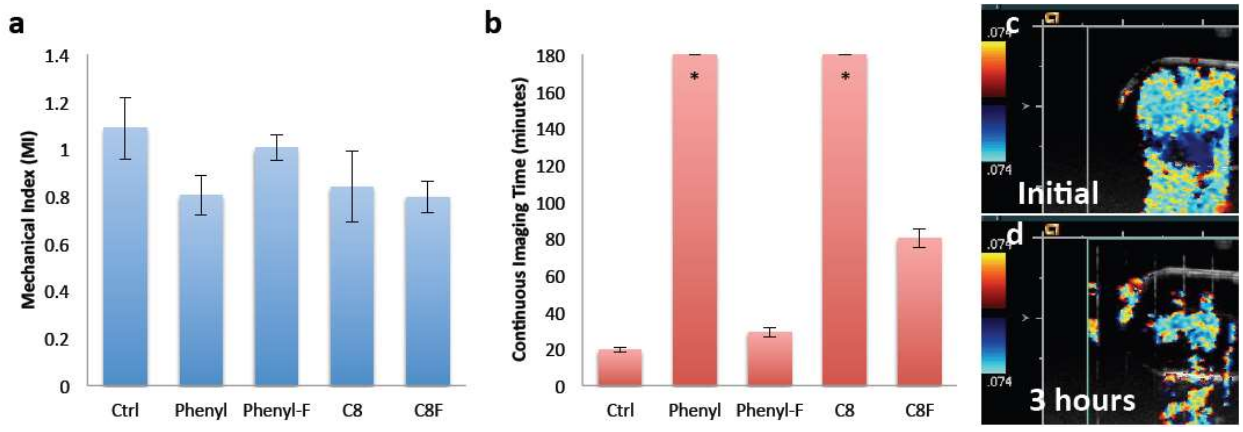

Figure 1.3 Color Doppler Ultrasound Testing of nanoshells.
A) Mean MI threshold to generate Color Doppler signal, the error bars signify standard deviation. B) Imaging lifetime in minutes of nanoshell formulations with continuous color Doppler imaging at MI=1.9, error bars signify standard deviations. *Note that the **Phenyl** and **C8** particles had no standard deviations because the test was terminated at 180 minutes. C) Color Doppler signal from **C8** nanoshells detected at the initiation of the continuous imaging study. D) Color Doppler imaging of the same **C8** suspension at 180 minutes. Note that although the signal decreases after 180 minutes, it was still robust. The long imaging times of the **C8** and **phenyl** particles correlate with these having the thinnest shell walls as shown in SEM and TEM imaging.

To quantitatively test the hypothesis that a different subpopulation of particles was being imaged at each MI, image brightness on contrast specific imaging was plotted over time (or frame number) for all the formulations; note this is a log scale. Figure 1.4A-B show signal brightness (blue curve) at each MI (green stepwise line) for the **control** and **phenyl** nanoshells. Note that signal increases as the MI is increased followed by signal decay as particles of a given sensitivity are consumed. Figures 1.4C-D are representative CPS ultrasound images of the **control** nanoshells at two different MI settings. Increasing the MI increases image brightness, which is seen as gold speckles on CPS imaging. As shown in Fig 1.4A-B, for an equivalent mass of particles, the **phenyl** particles are approximately twice as bright (on a log scale) at peak brightness compared to the **control** particles. Furthermore the signal in CPS mode does not experience as much signal decay for the **phenyl** nanoshells and persists at a brightness of 160 for several minutes compared to an immediate decay to below 40 for the **control** particles. The difference in imaging persistence between CPS imaging and color Doppler imaging is consistent with the CPS waveform being less destructive than the color Doppler waveform.

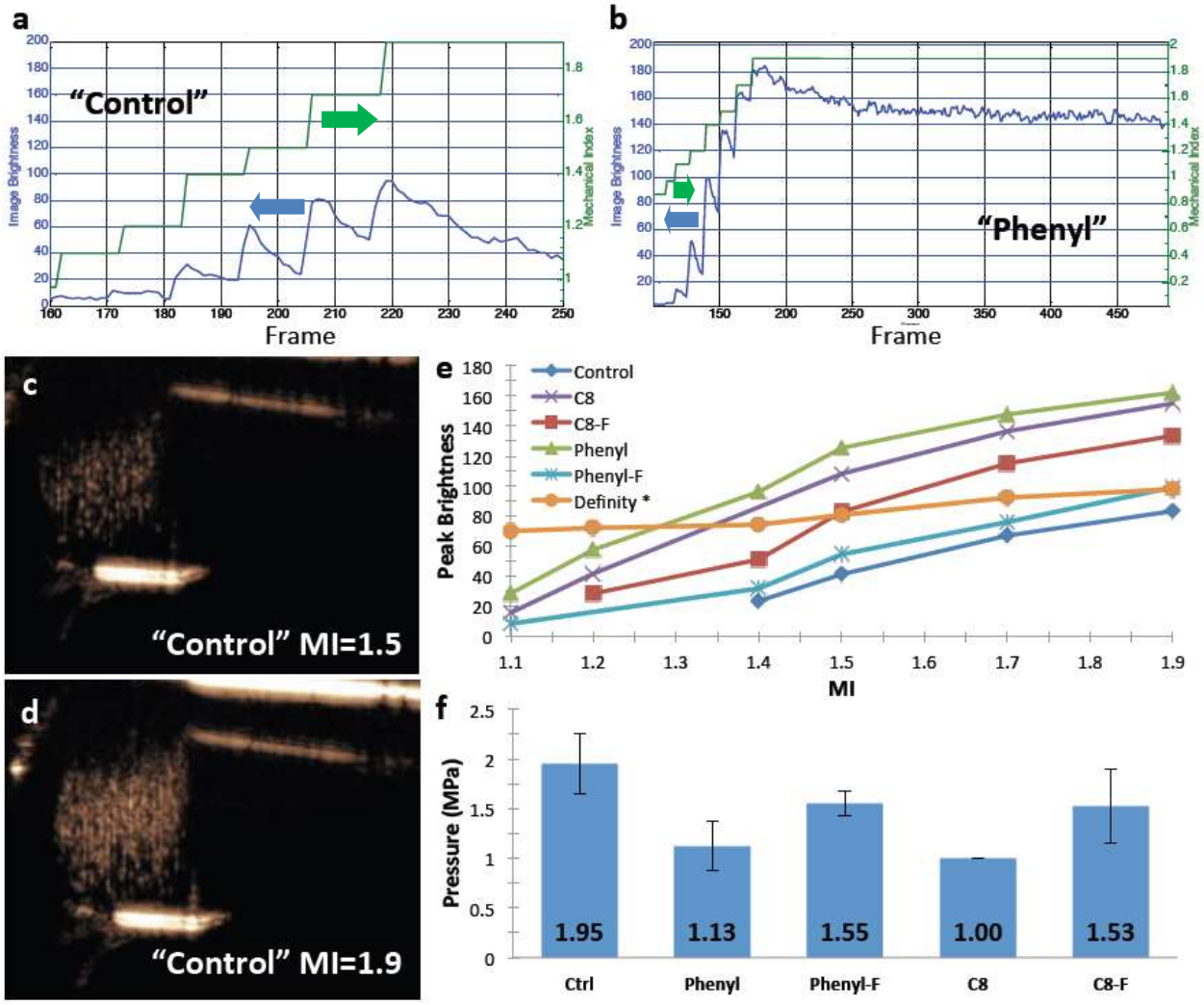

Figure 1.4 Image brightness over time with CPS imaging as a function of MI of PFP gas filled nanoshells. A) Signal brightness plotted with mechanical index as a function of time (frames) for **control** nanoshells. B**)** Signal brightness and mechanical index as a function of time (frames) for **phenyl** nanoshells. Note that with each MI step, brightness increases and then decays until the next MI step. Also note the greater signal generated with the **Phenyl** formulation at each MI and the slower decay even at maximum MI of 1.9. C) CPS image of **control** nanoshells acquired at MI = 1.5 D) CPS image of **control** nanoshells acquired at MI = 1.9. Note the greater brightness at 1.9 MI. E) is a plot of peak brightness on CPS images as a function of MI for all formulations. Note that the Phenyl formulation had a relatively low threshold and generated the brightest signal at all MIs. *Note: The sample gas volumes occupied between the nanoshells and Definity™ are equal; however; the Definity™ particle count is 64 times less than the nanoshells due to their larger size. F) Pressure threshold of the HIFU pulse that generated signal on the CPS image. Error bars signify standard deviations, N = 5. It should be noted that the brightness is log compressed.

Figure 1.4E shows peak brightness as a function of MI for each formulation; **phenyl**, **C8**, and **phenyl-F** formulations produced signal at lower thresholds compared to other formulations, and the **phenyl** and **C8** formulations produced the brightest signals. Note that ultrasound signals are log

compressed to display the entire dynamic range on the video monitor. Therefore the observed differences in brightness, as shown in Figure 1.4, are quite large.(83) Previous reports suggested that the peak-decay behavior of the control nanoshells at varying MI (as shown in Figure 1.4A) are consistent with the control particles having different subpopulations with varying mechanical strengths. The present data is consistent with different R-substituted trialkoxysilanes decreasing the average mechanical strength of the nanoshells, thereby allowing a brighter signal as well as an increased imaging longevity. For comparison, commercially available Definity™ microbubbles were diluted to an approximately equivalent gas volume as occupied by the nanoshells and compared directly to the nanoshells. This was done by particle volume because on average individual Definity™ microbubbles have a diameter between 1-3 microns, which results in a 64 times greater volume per particle than the nanoshells. It should be noted that in this MI regime, Definity™ microbubbles are being destroyed similarly to the nanoshells. However, unlike the nanoshell samples where the MI was slowly raised from 0.06 to 1.9 for each sample, each measurement on Definity™ microbubbles at each MI was done using a pristine sample due to the short imaging lifetime of Definity™. An MI of 1.9 is the maximum power used on clinical ultrasound imaging systems. It is evident from this data that the **C8** and the **phenyl** nanoshells generate more contrast at MIs greater than 1.3 than Definity™. To the authors' knowledge this is the first report of any rigid particle demonstrating a signal comparable to a commercially available contrast agent in a contrast specific imaging modality. This illustrates the unique properties than can be generated from nanostructures made of the ultrathin nanoflakes.

To determine the factors that influence the ultrasound signal threshold and intensity, 20 μs pulses at 1.1 MHz were delivered to the sample by the HIFU transducer to fracture and release the PFP gas as the sample was simultaneously being imaged in CPS mode at 0.1 MI to detect the freed PFP bubbles using the apparatus shown in Figure 1.1. Note that the 0.1 MI power is well below the signal generation threshold for all the formulations (Figure 1.4E). As shown in Figure 1.4F, all the formulations synthesized with the R-substituted trialkoxysilanes had a lower pressure threshold compared to the

control nanoshells. The **C8** nanoshells had the lowest pressure threshold, but this was not statistically different from the threshold of the **phenyl** nanoshells, both of which had a threshold approximately 50% that of the **control**. This demonstrates that use of ultrathin nanoflakes can be used for modify the mechanical properties of three dimensional structures. *Next the ultrathin shells were tested in vivo in VX2 tumor bearing rabbits.*

An in vivo experiment was performed in VX2 tumor bearing rabbits using a slightly modified ultrathin **phenyl** nanoshell formulation with a 55:45 molar ratio of trimethoxy(phenyl)silane: TMOS ratio. This ratio was used due to improved synthetic yield. 100 µl of nanoshells at 4 mg/ml were injected intratumorally and imaged over the course of 13 days. As can be seen from Figure 1.5 the signal remains easily detectable through at least 11 days by color Doppler imaging. Previous work by our group describes the control particles as having lasted for 10 days in PY8119 epithelial breast tumor bearing mice, and pure silica particles lasting in rabbit thighs after intramuscular injection for only 4 days.(32, 33) The current results are significant because unlike the mouse tumors, which are very poorly vascularized and isolated from motion, the VX2 model is well vascularized. These tumors were subject to extensive motion as the tumors were grown in the thigh muscles. Vascularization provides a means for both the particles and the encapsulated gas to escape. As a result, this figure demonstrates a significant improvement in performance over the previous iterations of nanoshells produced for ultrasound imaging.

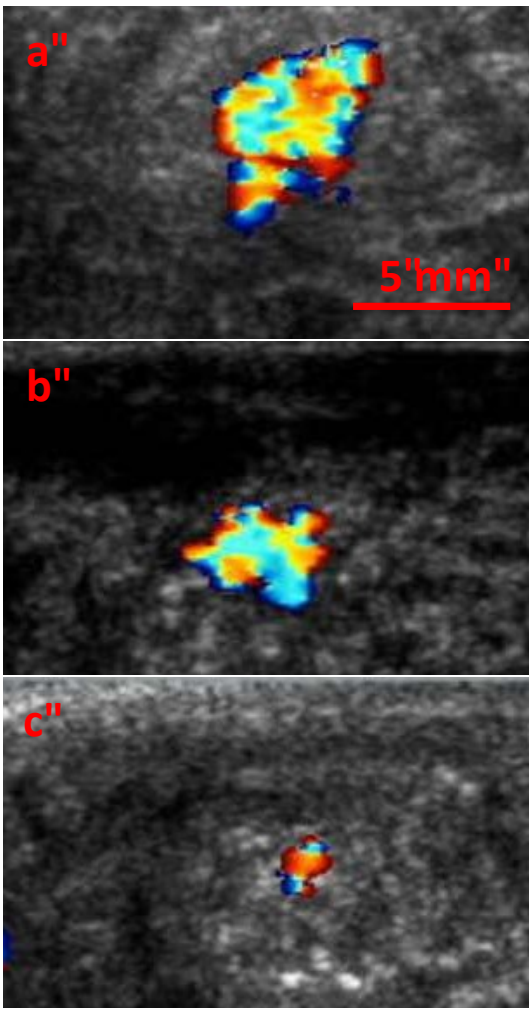

Figure 1.5 Intratumoral Nanoshell Longevity.
100 µl of nanoshells at 4 mg/ml were injected intratumorally into VX2 tumor bearing rabbits and imaged over the course of 13 days. A) 1 day after injection. B) 6 days after injection. C) 11 days after injection.

To further investigate the source of the mechanism of improved ultrasound performance, TEM imaging was performed. The images in Figure 1.6 are consistent with all formulations of nanoshells being composed of fused silica nanoflakes, which are linked together by condensation of surface silanol groups after they assemble on the template surface. These nanoflakes are formed initially during the sol-gel process and are present before calcination (See TEM image of control particles nanoflakes in Supplemental Figure 1.2). As can be seen from the TEM images, there is no clear pore structure throughout the nanoshells; it likely that the PFP gas which fills the particles enters through the grain

boundaries between weakly linked nanoflakes. As shown in Figure 1.6, the formulations synthesized with R-substituted trialkoxysilanes had markedly thinner shells than the **control** formulation and, therefore, are denoted as ultrathin nanoshells. The thinner walls of the ultrathin nanoshells result mechanically weaker shells than the thick walled **control** nanoshells. One potential source of the variation in structure and properties observed could be from varying degrees of reactivates or varying degrees of polycondensation between the different alkoxysilanes. These properties would result in different molar ratios of the organosilane incorporating to the silica shell rather than the starting amounts added. This could result in particles of different shell thicknesses, mechanical properties and differing sized nanoflakes. It is known that long chain alkyl and aromatic side groups of trialkoxysilanes will reduce the rate of hydrolysis and polycondensation due to their electron donating characteristic.(84) It has been shown that under neutral conditions without a catalyst (acid, base, metal alkoxides, etc.), triethoxy(octyl)silane undergoes very little hydrolysis which is necessary for polycondensation to occur.(85) Alternatively, the high electronegativity from the fluorination of these side groups creates a dipole about the silicon atom which leaves it more open to nucleophilic attack resulting in a higher degree of hydrolysis.(86) It is proposed that this would lead to a larger number of nanoflakes and thicker shell walls compared to non-fluorinated silanes.

There are at least three distinct regions in all of the nanoparticles. The inner dense layer is the black ring seen in images of all the particles (Layer A). The second layer is an intermediate less dense layer between the black ring and the middle loose silica flakes (Layer B). The final layer is an irregular corona of attached exterior silica flakes (Layer C). The **control** particles (Figure 1.6A-B) and the **phenyl-F** particles (Figure 1.6I-J) also appear to have a very thick Layer B. It is likely that the intermediate layer and the outer layer reduce the ultrasound performance of these particles. It should be noted that while the shell thickness appears to be the dominant property dictating the ultrasound activity of the nanoshells, it is not the only one. Other aspects that may play a role in the mechanical properties include the degree of condensation of the silica or the size of the nanoflakes that compose the particle shell.

The **C8** nanoshells and **phenyl** nanoshells have very similar ultrasound performance, but appear to have different nanostructures. Comparing the densest layer, whose fracture is postulated to occur at the minimum threshold, Layer A for the **phenyl** particles is 1.6 nm compared to 2.7 nm for the **C8** particles. Fracturing of the shell likely occurs during the rarefaction phase when the gas inside the nanoshell expands to uniformly apply pressure to the entire particle shell. By this metric, the **phenyl** formulation with the thinner Layer A should be significantly better than the **C8** formulation, but the standard deviation in shell thickness is greater in the case of the **C8** particles while the average shell thickness is approximately equal. Consequently, for **C8** particles the shell regions, where greater amounts of Layer C are absent and Layer B are minimal, may create weak shell fracture points since the pressure is applied uniformly through the shell. It is hypothesized that the additional differences in **phenyl** and **C8** particles performance may be due to their differing nanoflake structures.

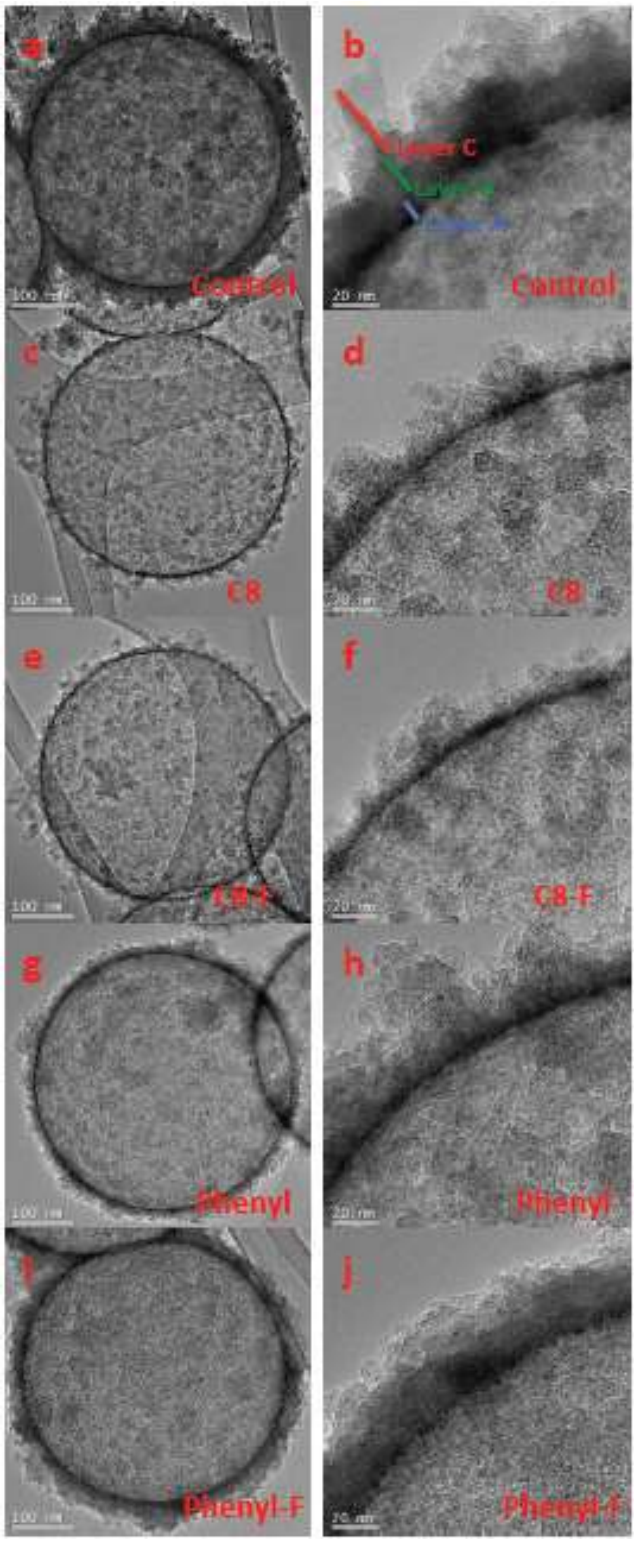

Figure 1.6 TEM images of all nanoshell formulations.
All images were taken at 40,000x magnification and then 150,000x magnification for high resolution images of the shells. A-B) **Control** nanoshells. C-D) Nanoshells synthesized with **C8.** E-F) Nanoshells synthesized with **C8-F.** G-H) Nanoshells synthesized with **phenyl.** I-J) Nanoshells synthesized with **phenyl-F**. The nanoshells synthesized with **C8 and phenyl** had the thinnest walls.

High magnification TEM images were used to further analyze the nanoflakes dimensions. For the nanoflake thickness, it was assumed that the Layer A thicknesses correlate to the thickness of individual nanoflakes. Nanoflake diameters were quantified using the nanoflakes orthogonally aligned to the nanoshells to understand the effect on ultrasound performance of the nanoshells. A smaller flake diameter may increase ultrasound brightness by formation more nanoflake junctions that can fracture. All the R-substituted trialkoxysilane formulations have decreased nanoflake diameters compared to the control formulations, as shown in Table 1.1. The **C8**, **C8-F**, and **phenyl-F** particles all had nearly identical nanoflake diameters and diameter standard deviations. It is hypothesized that the smaller flake diameters observed in the **phenyl** particles, 6.5 nm, compared to 8.9 nm for **C8**, may contribute to the differences observed in ultrasound performance, despite the nearly indistinguishable shell thicknesses between the two formulations.

Table 1.1 TEM based shell analysis

	Layer A (nm)	Layer B (nm)	Layer C (nm)	Sum Shell Thickness	Sum STD	Nanoflake Diameter (nm)	Diameter STD (nm)	Min Flake Diameter (nm)	Max Flake Diameter (nm)
Control	2.8	21.4	41.3	65.5	30.2	10.8	4.7	4.4	22.8
C8	2.7	5.6	14.3	22.6	12.2	8.9	2.6	4.5	15.6
C8-F	2.6	6.0	19.0	27.5	12.9	8.8	3.1	4.8	16.6
Phenyl	1.6	7.3	13.1	22.1	6.5	6.5	2.0	2.4	11.9
Phenyl-F	2.5	20.6	18.0	41.1	13.4	8.5	2.5	4.3	14.4

Twenty measurements were taken for each layer from multiple particles in Image J based on TEM images. Standard deviations for layers can be found in supplemental information. For Nanoflake measurements, fifty measurements were taken for each nanoparticle formulation in Image J from a minimum of four TEM images.

Conclusion

A method has been presented to prepare highly uniform three-dimensional structures composed of nanoflakes with thicknesses ranging from 1.3-3.9 nm and diameters ranging from 2.4-22.8 nm. This allows the synthesis of iron silica nanoshells of varying shell thicknesses with different mechanical

strengths. It was found that by using trimethoxy(phenyl)silane for 70% of the silicon source and the remainder tetramethyl orthosilicate, 500 nm hollow ultrathin nanoshells that had a dense inner shell thickness of only 1.6 nm could be synthesized. Combining alkyl(trialkoxy)silane precursors with tetramethyl orthosilicate reduces the building block size of the average nanoflake diameter in the shell wall by as much as 40% to 6.5 nm. The ultrathin nanoshells synthesized with these modified silanes were mechanically weaker and exhibited improved performance as ultrasound contrast agents *in vitro.* Compared to **control** nanoshells synthesized with only TMOS, the newly developed particles have a 10-fold increase in longevity during Doppler imaging. They also produce double the brightness during CPS imaging compared to **control** nanoshells, and became visible at a lower pressure threshold. The ultrasound data show that the ultrathin wall silica nanoshells have superior performance to commercial soft shell microbubbles for continuous imaging longevity in both Doppler and CPS imaging at clinically relevant powers. At an equivalent contained gas volume, the triethoxy(octyl)silane and trimethoxy(phenyl)silane substituted nanoshells generated greater contrast signal than commercial microbubbles at MI values exceeding 1.3 in CPS imaging. To the authors' knowledge, this is the first report of a rigid particle generating more ultrasound contrast at equivalent gas volumes than soft microbubbles at clinically relevant power settings. In vivo rabbit experiments demonstrated that the ultrathin nanoshells could retain stationary and produce color Doppler after 11 days after intratumoral injection in highly vascularized VX2 tumors. These results show that nanoflake precursors can be used to synthesize three dimensional ultrathin structures and thereby alter critical mechanical properties of the nanoshells.

Chapter 1, in full, is the material as it appears in Advanced Functional Materials in 2015. Liberman, A., James Wang, N. Lu, Robert D. Viveros, C. A. Allen, R. F. Mattrey, S. L. Blair, W. C. Trogler, M. J. Kim, and A. C. Kummel, 2015. The dissertation author was the co-primary investigator and author of this paper.

CHAPTER 2. EXTENDED LIFETIME *IN VIVO* PULSE STIMULATED ULTRASOUND IMAGING

In order to increase the *in vivo* lifespan of ultrasound contrast agents, hard shell silica nanoparticles with a diameter of 500 nm have been synthesized that can be used to encapsulate PFC gas or liquid (28, 32, 87, 88). It is proposed that a single high intensity ultrasound pulse converts the liquid droplet within the silica nanoshell to the gas phase via acoustic droplet vaporization (ADV). Ultrasound can superheat a PFC liquid droplet that is stabilized by a surfactant shell to vaporize into a bubble 100 times larger in volume than that of the original liquid droplet(89, 90). Apfel and Kripfgangs have reported applications of ADV in embolotherapy and drug delivery (89-93). Shi and coworkers have encapsulated perfluorohexane (boiling point = 56 ºC) in silica nanoshells as an enhancement agent for high intensity focused ultrasound (HIFU) therapy based on ADV (94). However, ADV applications specifically for ultrasound imaging with encapsulated perfluoropentane (PFP) liquid (boiling point = 29 ºC, Strem Chemicals) have only been studied in soft shell particles. For example, Sheeran *et al*. demonstrated that lipid encapsulated dodecafluorobutane nanodroplets could undergo ADV into micron sized gas phase bubbles at an ultrasound mechanical index (MI) of 1.2. This is within the FDA defined MI safety limit of 1.9 (95). Kripfgans *et al*. demonstrated that a single element transducer could be used to stimulate ADV of albumin coated microdroplets into gas microbubbles in a flow channel *in vitro* and could be imaged with B-mode ultrasound (90). A high frequency pulse could be used to convert acoustically transparent nanodroplets of lipid encapsulated PFP into B-mode visible microbubbles *in vivo* after intratumoral injection in mice grafted with hepatocellular carcinoma (93); however, non-linear imaging, such as contrast pulse sequencing (CPS), was not demonstrated. Thus, current research in ADV has been primarily focused on PFC droplets within soft and flexible lipid or polymer shells, which lack the *in vivo* stability of the hard shell silica nanoshell particles.

In this study, a novel imaging platform is reported for liquid PFC filled 500 nm rigid shell silica nanoparticles using single pulse stimulated imaging (SPSI) to generate an ultrasound CPS signal that is

visually comparable with commercial ultrasound contrast agents. While, conventional ultrasound contrast agents exhibit short *in vivo* lifetimes (< 30 minutes)(96, 97), liquid PFP core silica nanoshells represent the first type of on-demand ultrasound contrast agents with lifetimes that extend beyond several days of imaging time. Surface modification of the silica shell to target specific biomarkers such as folate extends the *in vivo* imaging lifetime by a factor of 4 times to 12 ± 2 days, which allow the biomarker to be injected at the time of biopsy even 1-2 weeks before surgical resection. This enables a new ultrasonic imaging modality with tumor enhancement and may permit time-dependent tumor development diagnosis and surgical guidance applications. The advantage of ADV with rigid shells is that they are chemically stable in tissue and can provide ultrasound signal when triggered. Surface functionalization increases tumor tissue retention up to several hours or even days after injection in contrast to soft shell nanoparticles with a short in-vivo lifetime under thirty minutes.

Material Characterization.

In vitro ultrasound experiments were performed to characterize the silica nanoshells. Scanning electron microscopy (SEM) was used to verify the spherical structure of the nanoparticles (Figure 2.1.) Based on transmission electron microscopy (TEM), the particles exhibit a mean diameter of 411 ± 17 nm. The *in vitro* CPS ultrasound at MI= 1.9 and color Doppler signal demonstrated that the silica nanoparticles were suitable for imaging based on the strong CPS contrast and color Doppler signals (Figure 2.1.) Under high mechanical index (1.9) ultrasound power insonation, a large population of nanoshells are simultaneously imaged. The high reflectivity of the nanoshells results in a significant degree of color Doppler shadowing that is characteristic of a long Doppler tail (33).

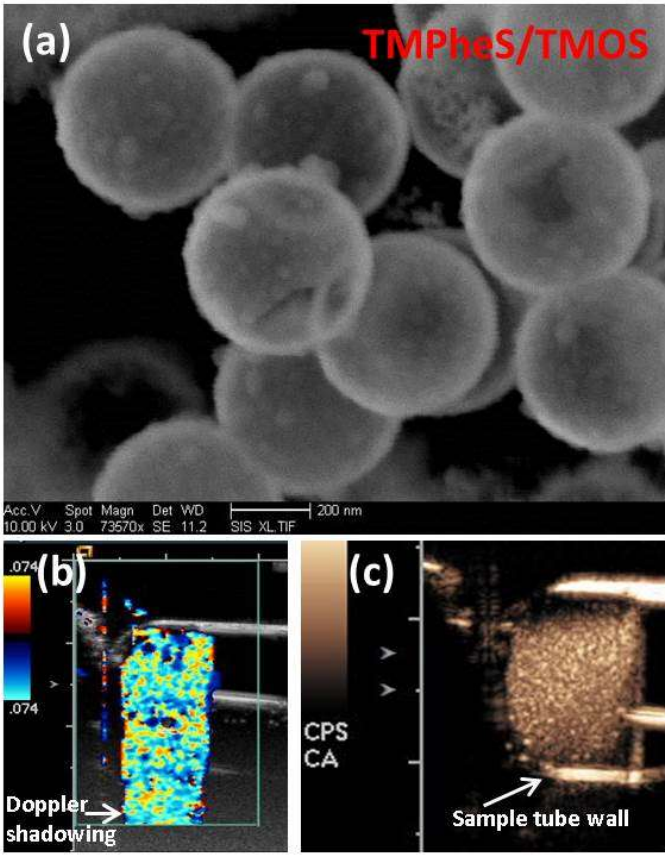

Figure 2.1 Silica nanoparticle characterization and performance.
(a) SEM images (b) Color Doppler imaging (c) CPS imaging.

Murine Tumor In Vivo Ultrasound Imaging.

In contrast to microbubbles, the rigidity of the calcined silica nanoshells results in long-term *in vivo* stability that offers long-term image guidance and tumor detection. In contrast to soft shell encapsulated PFP, the nanoshell particles are small enough to exhibit the enhanced permeability and retention (EPR) effect to passively accumulate in leaky tumor vasculature and become retained as demonstrated in previous work (33). Hashizume *et al* have demonstrated that the endothelial walls of leaky vasculatures in tumors have pore openings up to 2 µm in diameter originating from poorly connected, branched lining cells (98). Danquah *et al* also found that tumor vessels had endothelial openings from 0.1 to 3 µm (99, 100). Similarly, Yuan *et al* have found that the pore cutoff size ranges between 400 – 600 nm and Hobbs *et al* mentioned that the pore cutoff size of most tumors ranges from

380 – 780 nm (101, 102). As a result, 500 nm nanoshells may likely migrate through tumor endothelial pore openings that are large enough for extravasation and accumulation. Conventional lipid or polymer shell based microbubbles are short-lived and cannot be used for ultrasound imaging after several minutes(96, 97). Thus, microbubbles are usually used for tumor vascular blood flow studies based on real-time vascular perfusion.

Figure 2.2 (a) illustrates the ability of the silica nanoshells to accumulate at the tumor site, which is attributed to the EPR effect. After initial IV tail vein injection in the SHO mice grafted with LnCAP prostate adenocarcinoma, the mice were imaged daily with ultrasound CPS imaging and SPSI mode (Figure 2.2 (a)).

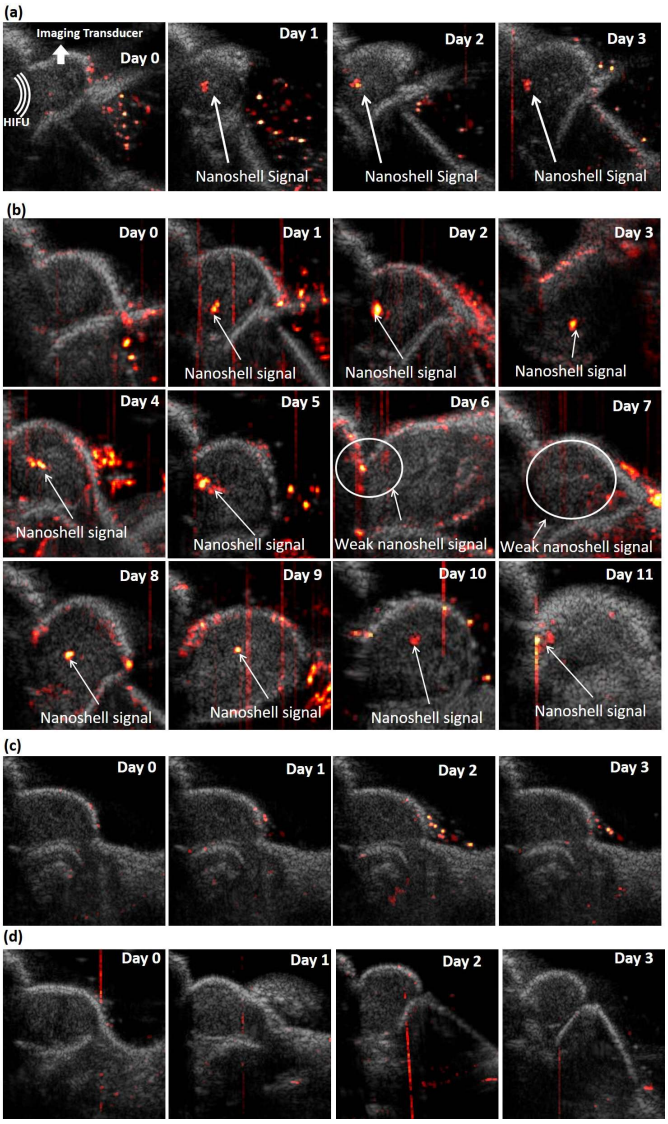

Figure 2.2 Representative stimulated CPS of nanoparticles in tumor over time.
The CPS signal was detected 20 μs after the HIFU pulse (a) Without folate functionalization (b) After folate functionalization. (c) Control experiment with injected with nanoshells but without HIFU pulse stimulation (d) Control experiment with no nanoshell injection and stimulated with HIFU pulse

It has been demonstrated in previous work that IV injected radiolabeled nanoshells accumulate in the tumor, as well as the liver (33). Thus, the nanoshells were expected to accumulate at the tumor site after IV administration in the present study. The mice were imaged with CPS and SPSI ultrasound daily after the initial injection. Figure 2.2 (a) shows that when a single high intensity ultrasound pulse is delivered to the tumor, the particles can be activated and imaged by CPS ultrasound imaging. The signal lifetime after each high intensity ultrasound pulse lasts for 1 second. Note this is a different measurement

than continuous HIFU induced imaging at a single spot which last over 5 minutes *in vivo*. Without the triggering ultrasound pulse, however, the particles remain dormant and do not interfere with traditional ultrasound CPS ultrasound tissue imaging. In contrast, tumors without nanoshells injection do not exhibit any CPS signal under pulse stimulation (Figure 2.2(d)). Furthermore, control experiments with injected nanoshells but no HIFU pulse, and no nanoshells but with HIFU pulse throughout a period of 2 weeks have shown no CPS signal from the tumor. Since each HIFU pulse has a duration of 20 μs, animal movement before and after the pulse can be negligible. However, because the mouse tumor cross-section is manually placed at the beam intersection of the ultrasound transducer and HIFU transducer, precise 3-D placement of is achieved but reposition at the same exact cross-section between daily timepoints is difficult. Note that stimulated CPS signal appears to be localized within the tumor. This is consistent with elevated tumor center interstitial pressure and low tumor peripheral pressure that results in localized distribution of nanoparticles in the tumor (103-105). Additionally, SPSI requires that the nanoparticle and imaging transducer maintain alignment for the stimulated CPS signal to be detected, thereby limiting the CPS signal generation events. The particles accumulate in the tumor site, remain stationary, and can be imaged for a mean of 3.3 ± 1 days as observed by SPSI. Figure 2.2 (a) is a representative image of a mouse over 3 days, which was taken from the cohort of 4 mice injected with non-functionalized nanoshells. The liquid PFP filled nanoshells still displayed strong CPS signals 3 days after initial IV injection. In contrast, conventional gas filled lipid or polymer based ultrasound contrast agents exhibit an imaging lifetime of less than 30 minutes (96, 97).

With EPR and active folate functionalization towards PSMA, which is up-regulated in the LnCAP tumor, the silica nanoparticle *in vivo* lifetime in the tumor is extended to a mean of 12 ± 2 days as detectable via SPSI (Figure 2.2 (b) and Figure 2.3). This significantly exceeds the 3.3 day imaging lifetime (Figure 2.3) when particle accumulation was based solely on the EPR effect. Figure 2.2 (b) is an 11 day representative image of a mouse from the cohort of 4 mice that received functionalized nanoshell injections. It can be seen with CPS that the folate functionalized nanoshells were stably localized within

the LnCAP tumor. PSMA in LnCAP tumors has been shown to exhibit folate hydrolase activity which mediates the cellular uptake of folate conjugated nanoparticles (106-108). Alternatively, activated macrophages could act as an ultrasound contrast carrier directed towards locally inflamed tissue. Inflammatory signals stimulate macrophages to express folate receptors and can also mediate internalization of folate-linked molecules (109, 110). Wong *et al* has further demonstrated that LnCAP cells activate and recruits macrophages via NFκB activation (111). An alternative hypothesis is that folate functionalized silica nanoshells could be internalized by activated macrophages that express folate receptors and then transported to the LnCAP tumor site or are better retained in the LnCAP tumor site by macrophages in the tumor.

To further quantify the CPS signal, particle average CPS image brightness decay over time has been characterized to compare the ultrasound *in vivo* lifetime between folate functionalized and non-functionalized nanoshells. A total of 12 mice with 4 mice for each group (folate functionalized nanoshells, non-folate functionalized nanoshells, no nanoshell injection) were analyzed for their CPS signal brightness with MATLAB. The CPS signal average brightness over time with standard deviation was plotted in Figure 2.3. It is found that after nanoshell injection, the particle begins to accumulate within the tumor and reaches maximum image brightness at the second day, which corresponds to maximum particle accumulation in the tumor. *In vitro* experiments have shown that higher particle concentrations result in higher image brightness. Non-functionalized nanoshells began to slowly wash out over day 3 and 4. Starting from day 5, no signal could be observed in any mice injected with non-functionalized nanoshells. In contrast, functionalized nanoshells displayed an extended *in vivo* signal for a mean of 12 ± 2 days. Since an interstitial pressure gradient exists from the tumor core decreasing towards the tumor periphery, non-functionalized nanoshells may wash out of the tumor (112). Tumor specific targeting may increase the nanoshell retention within the tumor tissue, thereby lengthening the *in vivo* imaging time. Functionalization is often thought to have minimal effect in delivering large nanoparticles to tumors(113); however, here the effect of functionalization is significant. This is attributed to enhanced nanoparticle

retention by the tumor after escape from the vasculature. The decrease in image brightness over 12 days for the folate nanoshells is consistent with the combined results of slow PFP diffusion into surrounding tissue, and particle exhaustion due to the daily application of pulsed imaging. There is a considerable amount of noise in the signal decay over time that may be attributed to mouse movement and the variance in relative imaging location. The similarity in maximum image brightness observed on the 2nd day (Figure 2.3.) between the folate-functionalized and non-functionalized particles suggests that folate-functionalization does not increase accumulated particle concentration within the tumor. While EPR appears to be the dominant targeting mechanism, folate functionalization promotes an extended tumor retention time and resulting imaging longevity.

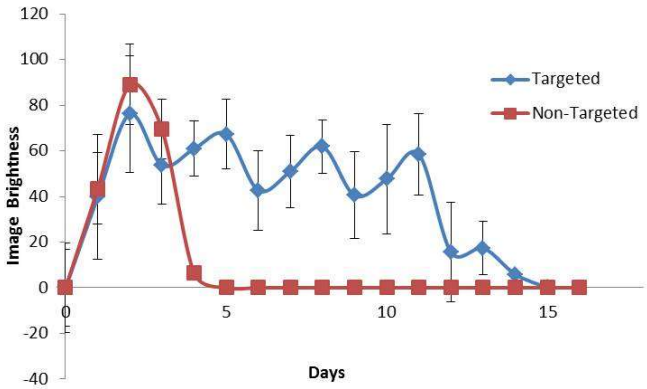

Figure 2.3 Image brightness vs time.
Image brightness of functionalized particles and non-functionalized particles in mice measured over time. The error bars represent standard deviations. The standard deviations include the variability of placing and aiming the HIFU and imaging transducer with respect to each other as well as to the tumor

In Vivo Biodistribution.

To further explore how the injected nanoshells accumulate within the tumor, nanoshells were radiolabeled with In^{111} via DTPA surface conjugation and IV injected into mice through the tail vein. Mice were euthanized and anatomized for single organ gamma scintigraphy measurement (Figure 2.4) on day 5 where the ultrasound image signal for non-functionalized nanoshells have completely diminished (Figure 2.3). To account for different organ and tumor weights, the scintigraphy counts were normalized

to the tissue weights and total injection amount for percent injection per gram. The biodistribution histogram show 1.92 times increase in tumor retention percentage for the functionalized nanoshells compared to non-functionalized nanoshells at day 5 (2.28% ± 0.43% vs 1.19% ± 0.52%). The detected In^{111} signal from the tumor further confirms that nanoshells are present in the tumor and can be stimulated for producing a CPS signal using a high intensity ultrasound pulse.

The large splenic and liver accumulation is attributed to macrophage phagocytosis and has been found in other studies on nanoparticle biodistributions (114). Weissleder has shown that nanoparticles ranging from 10 – 300 nm exhibits large liver and splenic accumulations while particles larger than 1000 nm accumulates in the lung (114). Similarly, Kumar showed that synthesized organically modified silica particles at 20 nm appear to accumulate mainly within the spleen after IV injection (115). Xie has further shown that 20 nm silica nanoparticles accumulate within the liver (30.31%) and spleen (27.32%) 7 days after IV injection (19). Their tissue histological analysis confirmed that the liver and splenic accumulation is due to macrophage phagocytosis (19). Godin found that 600 nm porous silicon discs mainly accumulate within the liver, yet 1700 nm porous silicon discs showed increased amounts of accumulation within the spleen (116). Immunohistochemical analysis demonstrates a higher association with macrophages (116). Our nanoshells are 500 nm, Fe (III) doped silica nanoparticles that are biodegradable via the Transferrin-Fe (III) chelating mechanism and fall within the size range for large liver and splenic accumulation due to macrophage phagocytosis. Furthermore, the biodistribution profile would be affected by nanoshell surface charge and tumor type that modulates macrophage quantity within the tumor stroma (114, 115, 117). It is acknowledged that the biodistribution may be distorted somewhat by the amount of radiolabel that detaches from the surface of the nanoshell (33). Additionally, our previous toxicology studies have shown that the nanoshells are cleared from mice within 10 weeks with minimum toxicity. Due to the iron doping and accumulation in the liver based on biodistribution studies, it is likely that the nanoshells are cleared via hepatic clearance. Since nanoshells are hollow, 3 times more silica nanoshells compared to solid particles can be injected for equal dosage based on mg/kg (118).

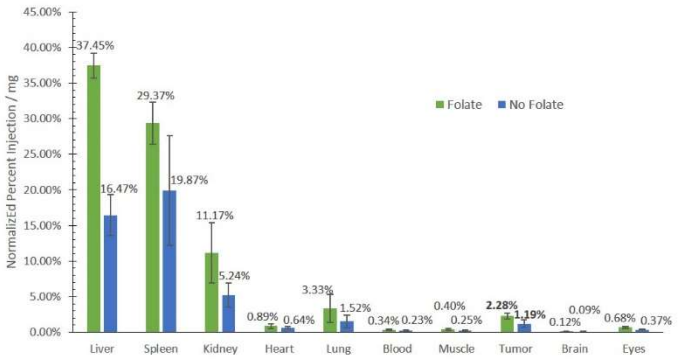

Figure 2.4 Biodistribution of nanoshells.
Biodistribution of folate functionalized nanoshells and non-folate functionalized nanoshells 5 days after IV injection. The normalized percent was determined by percent radiation normalized to total injection and normalized to tissue weight.

Ultrasound Imaging Mechanism.

In vitro ultrasound experiments were performed on liquid PFP filled 500 nm silica nanoshell particles and observed by TEM (JEOL 1200 EX II) at different ultrasound insonation pressures in order to elucidate the ultrasound imaging mechanism (Figure 2.5) of the silica nanoshell particles.

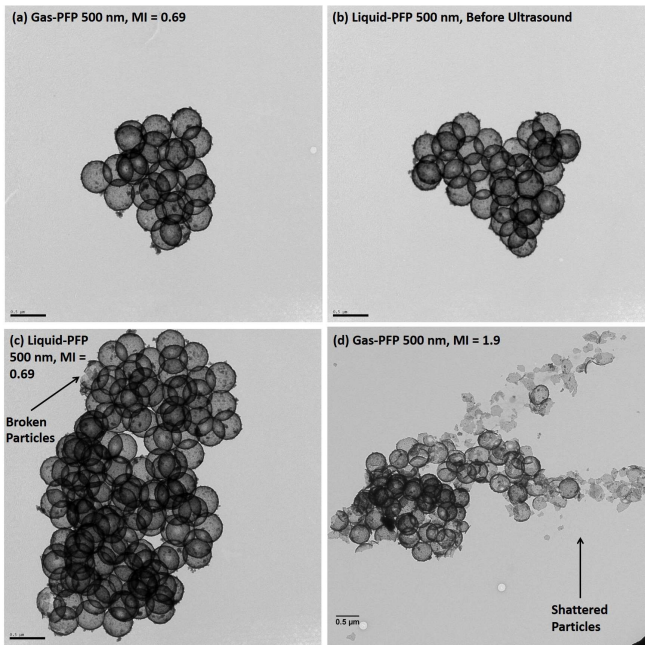

Figure 2.5 TEM of nanoshells in different regimes.
(a) Gas-PFP filled 500 nm nanoshells exposed to low ultrasound power, MI = 0.69 (1.83 MPa). (b) Liquid-PFP filled 500 nm nanoshells before ultrasound insonation. (c) Liquid-PFP filled 500 nm nanoshells exposed to low ultrasound power at MI = 0.69 (1.83 MPa) for 24 hours. (d) Liquid PFP filled 500 nm nanoshells exposed to high ultrasound power at MI = 1.9 (5.03 MPa) for 24 hours. The population of shattered nanoshells are pointed out with the black arrows.

At high ultrasound power (MI = 1.9, 5.03 MPa), the Doppler ultrasound signal persisted for 24 hours of continuous imaging before completely extinguishing. TEM showed that 43.4 % of the nanoshells were shattered. This is consistent with the strong ultrasound signal originating from inertial cavitation that fragmented the nanoshells at high ultrasound power (Figure 2.5 and Supplemental Figure 2.2). In contrast, liquid PFP filled 500 nm silica nanoshells were exposed to low ultrasound power (MI = 0.69, 1.83 MPa) for 24 hours. Under TEM, nanoshells exposed to low ultrasound power appears identical to nanoshells that were not exposed to any ultrasound insonation.

Table 2.1 Nanoshell shattering percentage at different regimes.

	Before Ultrasound	**MI = 0.69 (Gas PFP)**	**MI = 0.69 (Liquid PFP)**	**MI = 1.9 (Liquid PFP)**
Broken	0.16%	0.36%	0.35%	43.40%

Statistical analysis of liquid PFP filled 500 nm particles exposed to different ultrasound power regimes. Note that small holes are defined as holes with diameters less than 0.5 um. There were no shattered nanoshells before ultrasound exposure and after low ultrasound insonation (MI = 0.69). A total of 5343 particles were counted for the statistical measurement including at least 1100 for each category of particle collected from over several TEM images.

Conclusion

It has been shown that the 500 nm hard shell Fe (III) doped silica nanoshells are a strong ultrasound contrast agent with a long *in vivo* lifetime and are retained by tumors, which allows continued ultrasound imaging using CPS and SPSI. Their small size and ease of surface modification allows for accumulation or enhanced retention at the tumor site with passive targeting by the EPR effect and folate conjugation appears to mainly lead to increased retention at the tumor site after EPR accumulation. The hard shell silica nanoparticles minimized PFP diffusion from the shell to the bloodstream and enhanced stability in tissue, which resulted in long *in vivo* imaging lifetimes. In addition, the nanoshells were sufficiently fragile to be shattered with a single high intensity ultrasound pulse, which provides a new on demand imaging modality, SPSI. After IV injection in the mouse tail vein, the particles were observed by

SPSI to accumulate in the implanted tumor up to a mean of 3.3 ± 1 days post injection while not interfering with conventional diagnostic ultrasound imaging. Adding folate surface functionalization extended the *in vivo* SPSI imaging lifetime by a factor of four to a mean of 12 ± 2 days post injection. While functionalization is often thought to have a minimal effect in delivering large nanoparticles to tumors (113), here, the functionalization results in enhanced nanoparticle retention by the tumor. In contrast to the long lived *in vivo* ultrasound imaging attained in the present work, current clinically approved microbubble contrast agents exhibit an *in vivo* lifetime of less than thirty minutes (96, 97). SPSI in conjunction with the long-lived silica based ultrasound contrast agents represent a new class of ultrasonic imaging tools that can be applied to tumor localization and monitoring. Receptor-specific surface modification may further provide the important function of probing for molecular expressions in the tumor microenvironment (119-121) as well as localized drug delivery applications (122). The ultra-long lifetime enables ultrasound molecular imaging of early stage tumor development with biomarkers.

Chapter 2, in full, is the material as it appears in IEEE Transactions on Medical Imaging, 2017. Wang, James, Christopher V. Barback, Casey N. Ta, Joi Weeks, Natalie Gude, Robert F. Mattrey, Sarah L. Blair, William C. Trogler, Hotaik Lee, and Andrew C. Kummel, 2017. The dissertation author was the primary investigator and author of this paper.

CHAPTER 3. MICROSHELL ENHANCED ACOUSTIC ADJUVANTS FOR IMMUNOTHERAPY IN GLIOBLASTOMA

The present study examines the mechanism and efficacy of mechanical HIFU in combination with silica microshells loaded with perfluorocarbon (PFC) liquid to induce accumulation of immune-stimulatory cells within the tumor microenvironment and enhance the efficacy of anti-PD-1 therapy against advanced large glioblastoma tumors (123). Since glioblastoma is a fast growing tumor where treatment usually begins with surgical resection (123) , large advanced glioblastoma mouse tumor models most closely resemble clinical conditions. In addition, the large size allows the therapy to be tested on highly heterogenous tumors, which is a more stringent test than in most animal studies. The microshells provide a secondary application for image-guided ablation of solid tumors due to the presence of PFC, which is an inert, volatile compound commonly used in FDA approved ultrasound contrast agents as an acoustic reflector (124). These microshells were engineered to undergo inertial cavitation upon interaction with ultrasound and thereby augment cellular lysis and antigen release (73). Because glioblastoma is aggressively infiltrative, it is expected that microscopic disease remains in regions adjacent to the tumor after excision and is mainly responsible for tumor recurrence (125-128). An advanced subcutaneous model is used to approximate these microscopic remains after tumor resection. Note that a large opening in the skull is present in standard glioblastoma resection. In this context, it is proposed to directly inject the microshells into these adjacent regions, followed by focused ultrasound application (Scheme 1) and systemic checkpoint blockade therapy to establish in-situ vaccination against glioblastoma tumor formation from these infiltrative disease remains (127, 128). The paradigm of direct therapeutic delivery at the time of tumor resection is one that is widely adopted in several glioblastoma clinical trials. For example, engineered viruses and chemotherapies have been administered in this manner in several clinical trials (e.g. NCT01985256, NCT02798406, NCT02026271). Moreover, ultrasound is routinely used during surgery for intra-operative imaging since the bone opening easily accommodates the ultrasound probe (129). It is proposed to build on these established paradigms for the therapeutic application of

microshells and mechanical HIFU. Given the mechanical property of the cerebrum, it is anticipated that the microshells will remain at the site of the injection and not further penetrate into the tumor. However, the immune infiltrate that accumulates subsequent to PD-1 blockage and mechanical HIFU are expected to disseminate beyond the sites of microshell injection. It is hypothesized that the dissemination of subsequent immune reaction and related anti-tumor effects underlie the efficacy observed in the present study.

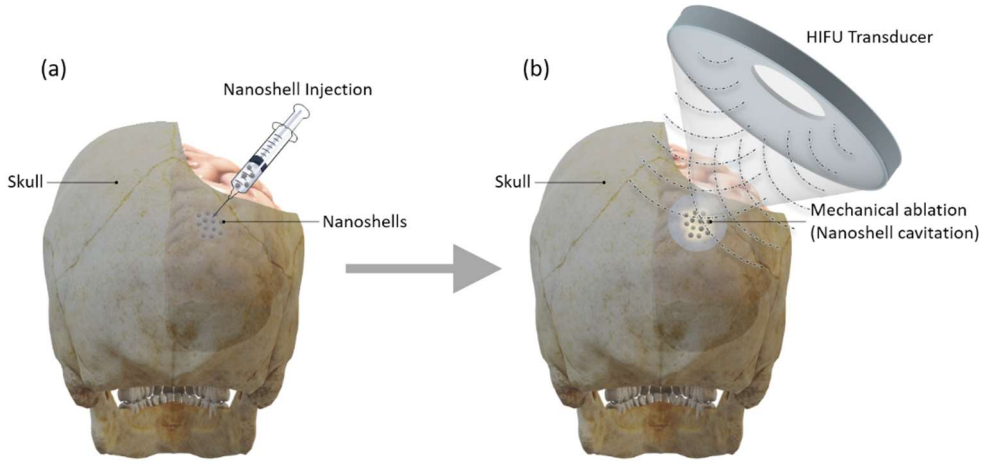

Figure 3.1 Schematic of Proposed Therapeutic Procedure
(a) Microshells are injected into the regions adjacent to the tumor after excision (b) HIFU mechanical ablation is performed on these regions with microshells. Systemic administration of PD-1 checkpoint blockade works synergistically with HIFU induced immune response to establish anti-tumor activity using the tumor margins. Penetration of the skull would not be necessary since the skull region overlying the tumor will be removed before surgical resection and microshell injection.

The effects of mechanical and thermal HIFU approaches were tested using ultra-thin walled silica microshells loaded with PFC liquid. Previous studies have shown that microshells with thinner walls require a lower acoustic threshold for ultrasound cavitation in diagnostic imaging (130). Herein, this concept is further applied for therapeutic ultrasound ablation (HIFU), where ultrathin walled microshells were used as cavitation sources that enable HIFU at low duty cycle and low acoustic pressure (131). The microshells provide a source for inertial cavitation via acoustic droplet vaporization (ADV) (90, 132, 133) to enhance cellular lysis, tissue damage, tumor antigen release and participate in converting a cold tumor microenvironment into a hot tumor microenvironment (73, 90). Additionally, the cavitation events

manifest as bubble clouds and can be observed with an imaging transducer that provides ultrasound guidance for mechanical ablation (76, 134).

Material Characterization

The use of liquid PFC filled silica microshells as an acoustic enhancer for HIFU was quantified by induced temperature response. Silica microshells were synthesized via a template-assisted sol-gel method (33). Phenyl modified silane groups were introduced as part of the silica precursor to create thinner shells (130). Based on TEM analysis, these monodisperse shells consist of a diameter of 1.5 ± 0.06 μm. It was hypothesized that since thermal HIFU (tHIFU) results in a temperature rise, then addition of silica microshells would further increase the temperature elevation due to cavitation induced vaporization of the PFC droplets. Microshells were initially vacuumed prior to PFP droplet loading. PFP liquid was incubated with microshells at a concentration of 50 μL per mg of microshells and then subsequently dispersed in water where the PFP droplets were trapped in the hollow core.

For a water solution without microshells, tHIFU insonation induced a temperature increase of 30 ºC. In contrast, water solution with microshell suspension resulted in a temperature rise from 0 to 60 ºC followed by a drop to 30 ºC (Figure 3.2a) when insonated by tHIFU. The high peak temperature rise is consistent with microshells enhancing tHIFU, while the temperature drop to 30 ºC is represents complete breakage (exhaustion) of all the microshells after 100 seconds of tHIFU under these conditions. Similarly, to test mechanical HIFU (mHIFU), the HIFU duty cycle was lowered to 2%, and water solutions with and without microshell suspensions were placed at the mHIFU focal zone. For both samples, only a temperature rise of 7 ºC was observed (Figure 3.2b), demonstrating that while microshells may have enhanced mHIFU efficacy, thermal effects were minimal. Comparatively, current clinical MRI guided intra-cranial ablation methods, such as laser ablation and thermal HIFU, both result in an elevation of temperature by at least 55 ºC (135, 136). With the presence of microshells as a carrier for acoustically active PFC paired with low HIFU duty cycle, mechanical ablation was achieved with only a 7 ºC

temperature rise at the region of interest, which is a factor of 6 less than clinically accepted methods. A TEM study was performed to evaluate if the tHIFU and mHIFU had fractured the microshells. For both tHIFU and mHIFU, the microshells were insonated for 2 minutes to reach the final state of the systems. TEM of the microshells before tHIFU or mHIFU show intact spheres (Figure 3.2c). Conversely, TEM of the microshells after both thermal and mechanical HIFU showed broken spheres, consistent with the HIFU induced inertial cavitation that causes shell fracture and can potentially be used for tissue or cellular lysis (Figure 3.2d).

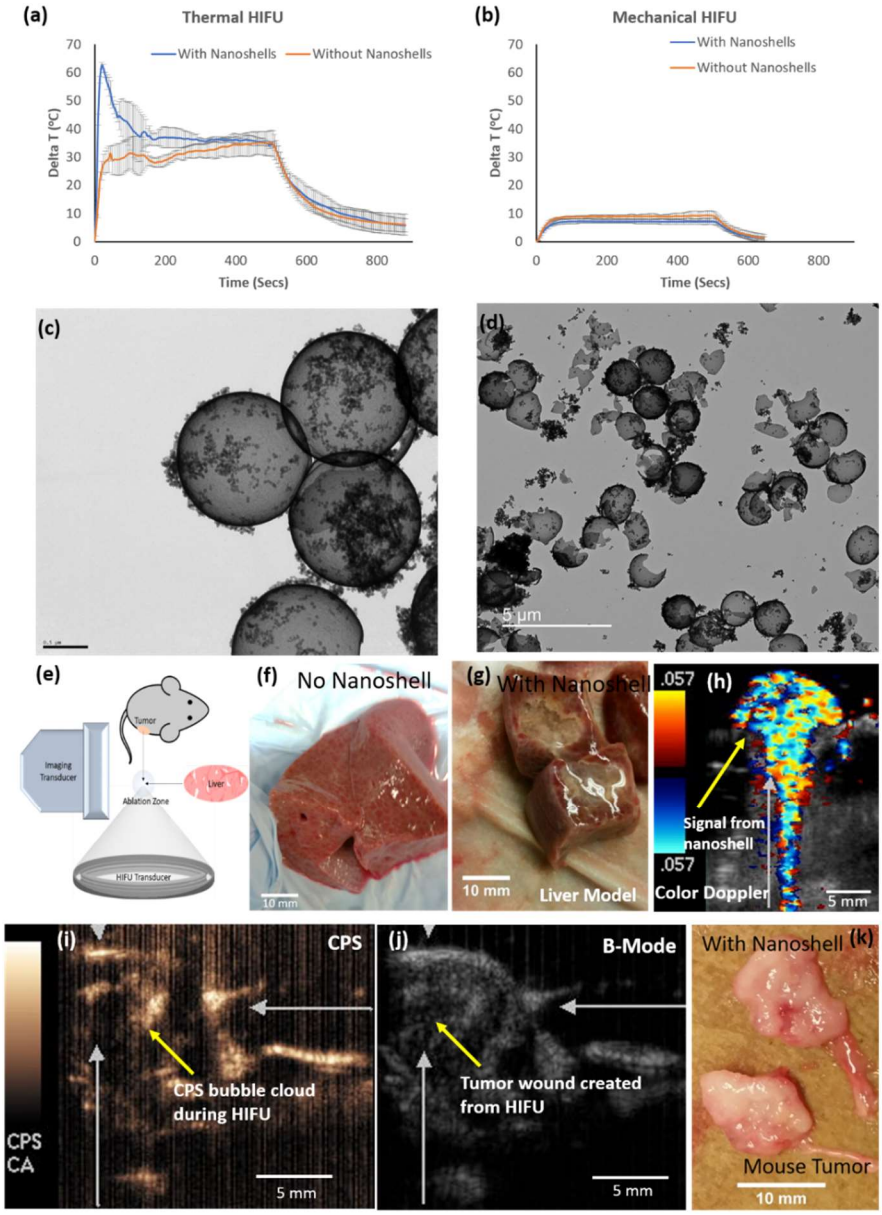

Figure 3.2 Microshell enhanced HIFU
(a) Microshell enhanced thermal HIFU: Microshells induced a maximum 60 ºC temperature rise in water compared to a 30 ºC temperature rise without microshells. After approximately 100 seconds, the microshells were exhausted resulting in identical temperature profiles. (b) Microshell enhanced mechanical HIFU. Microshells induced the same small temperature rise as the solution without microshells in water. (c) TEM of microshells before mechanical HIFU. Prior to ultrasonic cavitation, microshells appear intact and can be used to carry PFC liquid, which are strong acoustic reflectors (d) TEM of microshells after 2 min of mechanical HIFU. The mechanical HIFU shattered the microshells due to cavitational shockwaves (e) HIFU schematic detailing imaging transducer used for guiding the orthogonally placed HIFU transducer. (f) HIFU without microshells in ex vivo porcine liver. Note that the observed holes are the natural porosity in the liver. (g) Microshell enhanced mechanical HIFU resulted in a large tissue ablation area that is visible in the porcine liver when cut open. (h) Microshells showing a strong ultrasound color Doppler image for guidance purposes. (i) Bubble cloud formation of tumors with microshells enhanced mechanical HIFU visualized by ultrasound imaging. (j) Hypoechoic region in B-mode ultrasound of an ablated tumor wound that is visible with ultrasound. (k) Microshell enhanced mechanical HIFU in a mouse glioblastoma subcutaneous tumor (N = 3), resulting in a liquefied center that was observed after bisection.

It is expected that cavitation from fractured silica shells by mHIFU should be sufficient to induce tissue injury, which would in turn serve as foci for recruitment of immune cells (73). To determine if microshell assisted mHIFU induces tissue injury, silica microshells filled with liquid PFC were injected into porcine liver *ex vivo*. A diagnostic imaging transducer placed orthogonal to the HIFU beam path was used to guide the HIFU ablation. Simultaneous B-mode ultrasound imaging and contrast pulse sequencing permitted the microshell cavitation events to be superimposed on anatomical references from B-mode imaging. Tissue or mouse was manually adjusted in space to cover a large area of tumor for ablation (Figure 3.2e). For the porcine liver, treatment with mHIFU (with a 2% duty cycle) without the addition of PFC-microshells did not cause observable, gross tissue damage after 5 minutes (Figure 3.2f). In contrast, with the addition of PFC-microshells, a large region of tissue damage was readily observable after mHIFU treatment (Figure 3.2g).

To test for *in vivo* liquid PFC filled microshell assisted mHIFU tissue damage, direct injection within the tumor tissue in an animal model was employed (137). A direct intratumoral (IT) injection allows for sufficient concentration of 1.5 μm microshells within the tumor volume without the need for intravenous circulation that may restrict particle delivery to the tumors and thus require very large doses. It is also noted that the large tumors employed were likely heterogeneous and therefore not all of the tumor might be equally dosed if systemic injection were employed. To overcome the treatment resistance of heterogenous tumors, multiple microshell injections into the tumor were performed so that an immune response could be generated in all tumor microenvironments. By spreading the microshells spatially across the tumors, a better tumor remission response could be achieved, consistent with the multiple injections being able to be effective in a large heterogenous tumor. The GL261 murine glioblastoma cells were injected into the flanks of C57BL/6 mice and grown to large advanced tumors. Once a tumor had grown to about 500 mm^3 in volume, the PFC-microshells were directly injected into six different locations in each tumor. Six injections spatially distributed in the tumor volume allowed for a more uniform HIFU ablation throughout the tumor environment. Initial studies showed that spatially distributed

microshell enhanced HIFU exhibited a more favorable control on tumor size progression compared to single microshell injections. Because of the echogenicity of PFC, the injection site can be easily imaged by color Doppler imaging (Figure 3.2h). During mHIFU ablation on mouse flank tumors, bubble clouds were observed during HIFU ablation with contrast pulse sequence imaging (Figure 3.2i). The bubble clouds were characteristic of cavitation events induced by HIFU exposure. The consequent tissue injury could also be visualized with B-mode ultrasound imaging because the liquefied tissue is hypoechoic and appears as darker regions (Figure 3.2j). The region of the tissue injury was confirmed after removal of the mHIFU/PFC-microshell treated tumor (Figure 3.2k). The dark hypoechoic region visualized on B-mode ultrasound imaging. (Figure 3.2j) corresponded to the anatomic region characterized by liquefied tissue voids (Figure 3.2k). For subsequent *in vivo* efficacy studies, these bubble clouds were used as an ultrasound imaging marker to guide the ablation focal zone with an orthogonally placed ultrasound imaging transducer (Figure 3.2e and 3.2j).

In Vivo Characterization

Since microshell enhanced mHIFU can result in gross tissue damage without thermal effects, it was hypothesized that in the tumor, such zones of tissue injury can serve as foci for recruitment of immune-stimulatory cells. The lack of temperature elevation would ensure that tumor neo-antigens were not denatured. The relative abundance of T cells in the tumor microenvironment is an important determinant of response to anti-PD1 therapy (138) (Figure 3.3a). CD3 is expressed in all T cells and serve as a general marker for T cell activity (139). An immunofluorescence study was performed to determine if mHIFU/PFC-microshell with PD-1 blockade treatment induced the accumulation of CD3+ T cells *in vivo* (Figure 3.3b). Mice harboring subcutaneous glioblastoma tumors were treated with mHIFU/PFC-microshell with or without anti-PD1 antibody. While glioblastoma normally occurs in the brain, a subcutaneous model is an essential first step towards developing a protocol for cranial HIFU. With the same tumor models for radiation therapy, therapeutic effects observed in subcutaneous implantation correlates with treatment effects done on orthotopically implanted tumors (140, 141). Similarly, drug

injectables such as dichloroacetate, a kinase inhibitor for inhibiting glioblastoma growth, and micelle loaded paclitaxel have been studied in subcutaneous and intracranial mouse tumors and have shown correlation in tumor suppression between subcutaneous and intracranial tumors (142, 143). Therapy development that begins with a glioblastoma subcutaneous model allows for ease of tumor access for ablation therapy and frequent monitoring of tumor size, representative of time-sensitive treatment efficacy such as immune therapy. PFC filled microshells were IT injected into mice containing large advanced glioblastoma tumors (~500 mm^3) in the flank and subjected to mechanical HIFU ablation for 2 minutes, followed by administration of aPD-1 via intraperitoneal injection (IP) every two days for a total of six doses in ten days. Tumors were harvested at the end of the treatment and analyzed with fluoresence immunohistochemistry (Figure 3.3c). Initial treatment optimization studies showed that the average tumor growth deflection occurs around day 10 to day 15, which coincides with the end of the treatment schedule (Figure 3.3c). Consequently, day 10 was used to analyze the tumor-infiltrating immune cells. Rechallenge experiments were employed to determine the long term adaptive immune memory effects. Tissue fluorescent immunohistochemistry analysis showed that multiple foci of CD3+ immunofluorescence was seen only in tumors treated with mHIFU/PFC-microshell combined with anti-PD-1 antibodies (Figure 3.3b), indicating highly concentrated T cells infiltrating at the tumor site and localized at mHIFU ablation zones. The presence of highly concentrated T cells further confirms that minimizing thermal effects in HIFU tumor ablation can augment the immunostimulatory efficacy of PD-1 blockade.

While CD3 maps the infiltrating T cells in histology sectioning slides, 4 additional markers for other types of lymphocytes were studied with whole tumor cell population analysis. The tumor microenvironment was further examined for accumulation of CD45 leukocytes (Figure 3.3d), CD3 T cells, and CD8 cytotoxic T cells (which are considered to be the main effector cells for anti-tumor response, Figure 3.3e), CD 4 helper T cells and interferon gamma (IFNγ) expression (Figure 3.3f). A comparison across all five markers demonstrated a consistent increase in immune activity in the combination cohort

when compared to the other groups with monotherapies (mHIFU-NS + Isotype or aPD-1) and control. CD45 is a receptor that is linked to protein tyrosine phosphatase and is a marker for T cell activation (144). CD8 is a membrane protein that is a co-receptor to the T cell receptor and binds to the major histocompatibility complex (MHC) and is mainly expressed on the surface of cytotoxic T cells. IFNγ is a cytokine that is secreted by the CD8 cytotoxic T cells when acquired immunity develops and is a biomarker used to indicate the activity level of CD8 cytotoxic T cells. Tumor specimens were derived after mHIFU/PFC-microshell/anti-PD1 antibody treatment (or mono-therapies) and analyzed using FACS. For all three biomarkers of immune-activation, significant enhancement was observed when mHIFU/PFC-microshell treatment was performed in combination with aPD-1 treatment (Figure 3.3d-f). A triple effect was observed. (i) The proportion of CD45 leukocytes in the glioblastoma microenvironment was increased more than 20 fold by the combined mHIFU/PFC-microshell/PD-1 blockade treatment relative to each monotherapy (Figure 3.3d). (ii) The proportion of CD8 cytotoxic T-cells in the glioblastoma microenvironment was increased more than 100 fold by the combined mHIFU/PFC-microshell/PD-1 blockade treatment relative to each component treatment (Figure 3.3e). (iii) The expression of IFNγ was increased more than 200 fold after combined mHIFU/PFC-microshell/PD-L1 blockade treatment relative to each component treatment (Figure 3.3f). These results suggest that mHIFU/PFC microshells facilitated a “cold” to “hot” immune-microenvironment transition when combined with anti-PD1 checkpoint blockade.

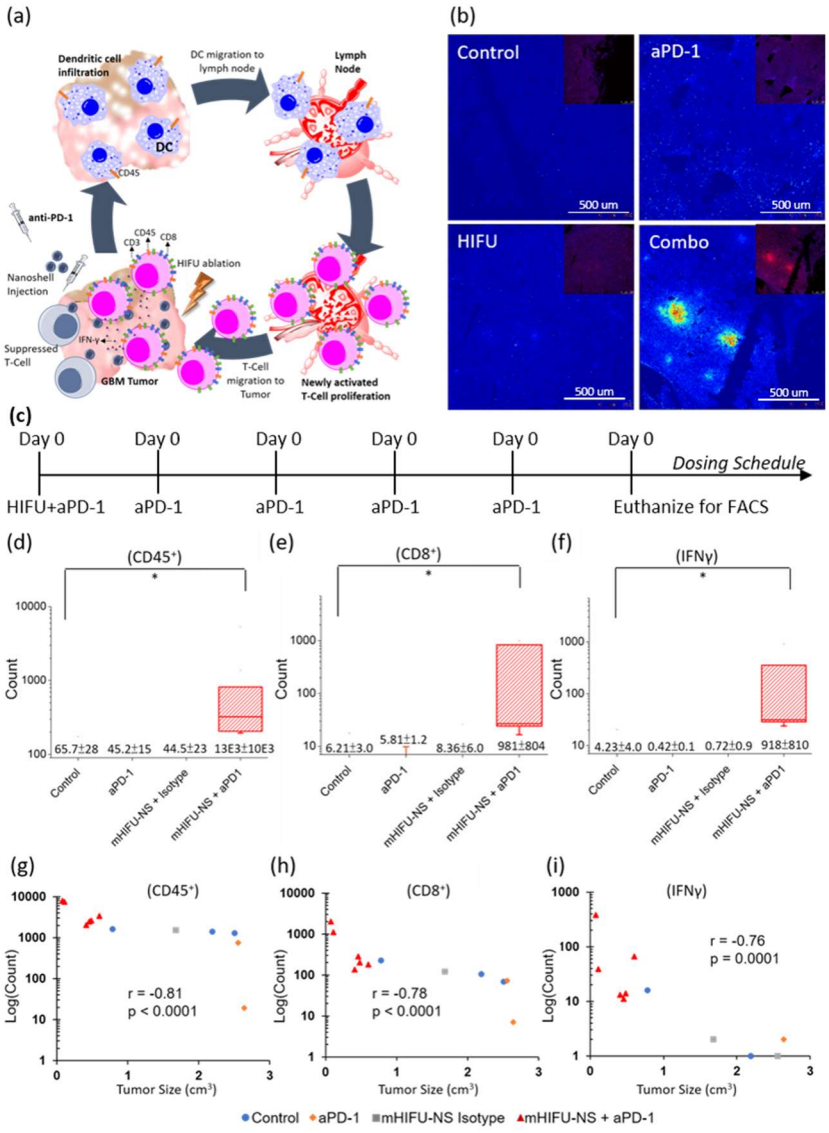

Figure 3.3 Immunohistochemical Analysis

(a) Proposed mechanism of acoustic based adjuvants for checkpoint blockade therapies. The GBM tumor is "cold" due to a suppressed immune microenvironment. Mechanical HIFU ablation enhanced by microshells (small blue spheres) are hypothesized to induce *in situ* cellular lysis via ultrasonic cavitation. The simultaneous PD-1 blockade prevents further immune cell suppression. Dendritic cells subsequently recognize tumor neo-antigens released from cellular lysis and stimulate T cell proliferation. Newly activated cytotoxic T cells (CD45+, CD3+, CD8+) transform the GBM tumor into a "hot" immune active microenvironment. (b) Immunohistofluorescence (IHC) staining of tumor-infiltrating CD3+ T cells and heatmap. Inset is where CD3 T cells are dyed in red while blue is the DAPI nuclear dye. The combination (combo, mHIFU-NS+aPD-1) group shows specific hot spots containing highly concentrated tumor infiltrating T-cells. A heat map was generated for better visualization (N = 6). (c) Treatment and sample collection schedule. A total of 6 PD-1 blockade doses were administered (1 loading dose and 5 maintaining doses) within 10 days. After the final dose of aPD-1, mice were euthanized for FACS analysis (d-f) Box chart showing CD45, CD8, and IFN- γ levels across cohorts (N = 6). The mice cohort that received combination therapy of mHIFU-NS with aPD-1 consistently exhibited increased levels of CD45, CD8 and IFN-γ when compared to monotherapies or control groups. (g-i) Spearman correlation plots of tumor size vs CD45, CD8 and IFN- γ levels across cohorts showing immune activity that correlates inversely with tumor size. Smaller size tumors showed increased levels of CD45, CD8, and IFN-γ, reflective of anti-tumor immunity.

A correlation between tumor size and immune response was also observed ten days after the treatment (Figure 3.3g-i). For CD45 analysis, smaller tumor sizes after mHIFU/PFC-microshell/anti-PD-1 treatment corresponded to larger populations of tumor infiltrating CD45 cells with a Spearman's correlation coefficient of -0.81($p<0.001$, Figure 3.3g). Similarly, tumor size inversely correlated with the CD8+ cytotoxic T-cell population (Figure 3.3h) in the glioblastoma microenvironment, and also IFN-γ (R^2=-0.86, p=0.001, Figure 3.3i). These results demonstrate that tumor regression after mHIFU/PFC-microshell/anti-PD-1 treatment is largely induced by an activated anti-tumor host immune response. The association between strong immune activity and small tumor size has also been demonstrated by other groups (145). Furthermore, increased IFN-γ levels were shown to result in suppressed growth of neuroblastomas (146). High levels of IFN-γ may induce expression of MHC class I antigens and concomitantly facilitate immune recognition of CD8+ cytotoxic T cells for anti-tumor activities (146), consistent with what was observed in the mice cohorts that received mHIFU/PFC-microshell/anti-PD-1 treatments.

In Vivo Survival Study

A tumor progression study was performed to determine if the transition from that of a "cold" to a "hot" immune-microenvironment induced by the combined mHIFU/PFC-microshell/anti-PD-1 treatment would be associated with enhanced anti-neoplastic effects. PFC-microshells were injected into mice subcutaneously grown with large advanced glioblastoma tumor in the flank (Tumor size of 500 mm^3 on average) and treated with combination or single therapies. Large advanced tumors were employed since they were expected to be the most resistant to immunotherapy treatment and most relevant to clinical settings. With mechanical HIFU or aPD-1 multidose monotherapies, implanted glioblastoma grafts grew at a rate comparable to the control groups (Figures 3.4b-d). In contrast, when microshell enhanced mechanical HIFU was combined with aPD-1, tumor remission was achieved in ~75% of the implanted glioblastoma grafts (Figure 3.4e). When thermal HIFU was combined with PFC-microshell and aPD-1 therapies, tumors continued to progress similarly to the control cohort (Figure 3.4f), suggesting that the

thermal effects were associated with tHIFU prohibiting immune-stimulation. The combined survival curves demonstrated that microshell enhanced mechanical HIFU combined with aPD-1 therapies resulted in a significantly improved survival rate of mice with glioblastoma tumors (Figure 3.4g).

A re-challenge experiment was performed to determine whether acquired immunity against cancer was achieved in the mice. When glioblastoma tumor cells was re-introduced into mice previous implanted and became tumor-free mice after mHIFU/PFC-microshell/aPD-1 treatment, no tumor growth was observed. *These observations suggest that the treated mice had acquired long-term immune memory to glioblastoma when microshell enhanced mechanical HIFU was combined with aPD-1 therapy.*

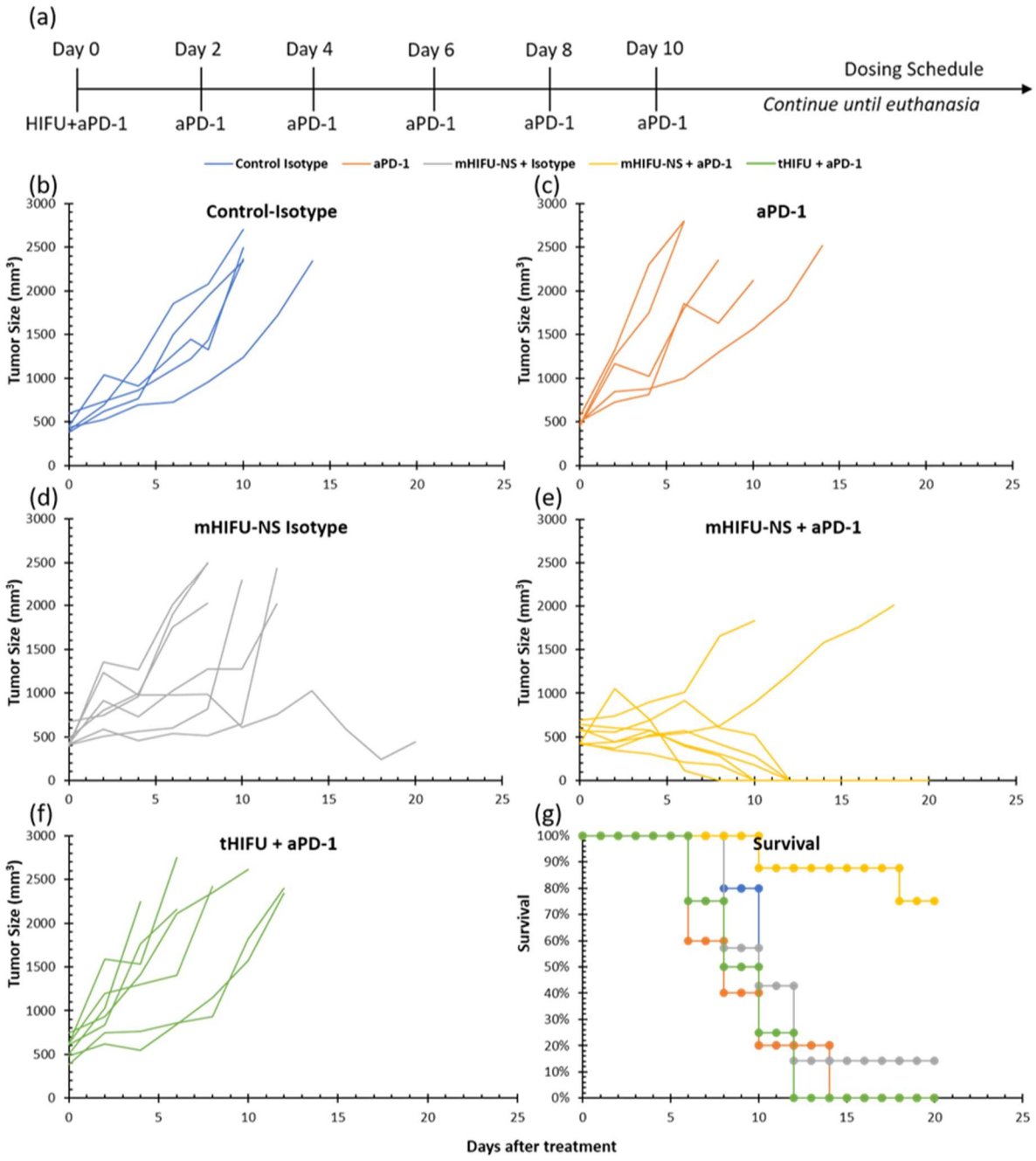

Figure 3.4 Tumor progression and survival curves

(a) Treatment schedule. A total of 6 PD-1 blockade doses was employed (1 loading dose and 5 maintaining dose) immediately after HIFU treatment (Day 0) and lasted for 10 days. (b) Individual mouse tumor progression curves for control isotypes. N = 5 (c) Individual mouse tumor progression curves for aPD-1 monotherapy. Current PD-1 blockade treatment plan did not result in tumor stabilization, but resulted in tumor growth similar to control cohorts. N = 5 (d) Individual mouse tumor progression curves for microshell enhanced mechanical HIFU with isotype monotherapy. Microshell enhanced HIFU resulted in minor level of tumor progression control. N = 7 (e) Individual mouse tumor progression curves for microshell enhanced mechanical HIFU with aPD-1 therapy. Microshell enhanced mechanical HIFU combined with PD-1 blockade resulted in 75% of tumor remission. N = 8 (f) Individual mouse tumor progression curves for thermal HIFU (tHIFU) with aPD-1 therapy. Tumor progression was similar to control cohorts. N = 7 (g) Percent survival after treatment. P value for tumor size at day 10 was <0.001. N = 26.

While immune checkpoint inhibitors have yielded strong clinical efficacy against a number of tumor types (52-57), application of this strategy to glioblastomas has been challenging (58). The available data suggest that glioblastoma harbors a "cold" immune microenvironment that lacks requisite immune cells for anti-PD-1efficacy. This work demonstrates the feasibility of converting this "cold" microenvironment to a "hot" micro-environment through mHIFU. When combined with intra-tumoral injection of PFC loaded silica microshell, mHIFU induced inertial cavitation of silica-microshells and caused local tissue damage. While these sites are presumed reservoirs for antigen release and damage associated molecular patterns (DAMPs), the immunosuppressive glioblastoma microenvironment prevents the recruitment of immune-stimulatory cells (i.e. CD45+, CD3+ or CD8+ cells) until anti-PD1 blockade is applied. After PD-1 has been inhibited, dendritic cells that recognize DAMPs and tumor neo-antigens migrate to the lymph node as matured antigen presenting cells (APCs), which stimulate cytotoxic T cell proliferation with tumor specificity. The newly trained cytotoxic T cells begin to migrate to the tumor microenvironment and are specific to the tumors, while the immunosuppressive PD-1 has been continuously inhibited. Subsequent accumulation of immune-stimulatory cells and IFN-γ expression induced anti-tumor immunity and led to tumor regression (Figure 3.3a).

The presence of silica based materials can stimulate an innate immune response via inflammasome activation (147); in addition, it has been reported that such inflammasome activation was crucial in stimulating a response against dying tumor cells, linking the innate immune pathway with the acquired immune pathway (148). In the present study, tumor re-challenge experiments suggested that the host had eventually developed acquired immune memory against glioblastoma tumors after combined microshell focused mHIFU and aPD-1 therapy. It is worth considering that the silica material also assisted in developing such acquired immune response.

When administered in combination with the PFC-microshells, mHIFU enhanced the efficacy of anti-PD1 therapy but tHIFU did not. This observation suggests that thermal escalation in the tumor

microenvironment compromised the host anti-tumor immune response. These findings were consistent with previous studies demonstrating that low-duty cycle mHIFU is more effective in stimulating immunological responses than tHIFU in melanoma and colon models (75). Excessive heat generation may induce protein denaturation or inactivation of cells that compromise antigen presentation and activation of immune response (75, 149). Note that thermal-based HIFU methods have already been developed with magnetic resonance guidance for several brain conditions such as glioblastoma (150), chronic neuropathic pain, essential tremor, and Parkinson's disease (135) and represents a potential non-invasive ablation method alternative to radiation or surgery in the brain. Furthermore, with the combination of ultrasound microbubbles, HIFU has been used clinically to distrupt blood brain barriers for more effective drug transport (135). For the present application, a strategy is proposed whereby the microshells are directly injected into the surgical resection cavity at the time of surgery. Since glioblastoma is aggressively infiltrative, microscopic tumor remains adjacent to the resection cavity can be used to re-stimulate the immune system. Penetration of the skull would not be necessary since the skull overlying the tumor will be removed before surgical resection and microshell injection (Figure 3.1). In this context, a subcutaneous tumor model was employed to provide proof-of-principle data for the proposed approach. Furthermore, since human glioblastoma exhibit significant regional heterogeneity in both genotype and phenotype (126-128), the immune reaction solicited in one region may not be optimal for destruction of tumor in another region. In this context, multiple intra-tumoral injections were performed to spatially distribute the microshells in distinct regions of the tumor, with the goal of soliciting a variety of immune reactions against the inherent glioblastoma heterogeneity. The efficacy observed in the present study supports consideration for clinical translation of this approach.

Conclusion

The present study has demonstrated that PFC filled microshells effectively provided a two-pronged approach to complement checkpoint blockade therapies. The presence of inert PFC droplets serves as a cavitation center to promote effective mechanical ablation with minimal thermal effects at low

HIFU pressure output while also serving as a source for ultrasound guidance. In the context of PD-1 blockade, the HIFU ablation sites accumulate one to two orders of magnitude of increase in immune stimulatory leukocytes and cytotoxic lymphocytes, thereby converting the immune "cold" glioblastoma microenvironment into a "hot" microenvironment to better facilitate checkpoint blockade treatments. This transition is associated with glioblastoma regression and induction of anti-tumor immune memory. This work suggest potential new opportunities where physical adjuvants such as acoustic ablation, that participate in immune pathway stimulation, can be tuned to combine with existing immunotherapies for cancer types that are not readily responsive to checkpoint blockade treatments.

Chapter 3 , in full, is the material as it may appear in Advanced Therapeutics, 2019. Wang, James, Ching-Hsin Huang, Oscar H. Echeagaray, Siamak Amirfakhri, Sarah L. Blair, William C. Trogler, Andrew C. Kummel, Clark C. Chen, 2019. The dissertation author was the primary investigator and author of this paper.

CONCLUSION AND RECOMMENDATIONS FOR FUTURE WORK

The feasibility of converting cold tumors into hot tumors to complement immunotherapy has been demonstrated in this work. The significance herein is the generalizability of a non-thermal, mechanical acoustic ablation platform that can be applied to other solid tumors that have not seen efficacy with immunotherapy.

Conclusions

The mechanical rigidity of silica shells have been shown to be tunable via adjustment of silica precursors which resulted in a difference in shell thickness. Ultrathin shells (1.4 nm in thickness) have been shown to exhibit ultrasound signal comparable to commercial microbubble contrast agents that are composed of lipid soft shells. Furthermore, ultrathin shells provide a 9x longer continuous Doppler imaging lifetime when compared to commercial microbubbles, offering potential extended period tumor marking or imaging functionalities. In mice grafted with subcutaneous tumor, these silica shells are imageable at concentrations of less than 10 μg in the tumor and up to 2 weeks with folate targeting. In contrast, commercial microbubbles have a life time of 20 - 30 minutes. When injected directly into the tumor, the ultrathin silica shells act as an ultrasound proxy for image guided ablation. They further decrease the required acoustic power, resulting in tissue ablation occurring only where the nanoshells are located within the tumor, increasing general safety margin. When the nanoshell enhanced ablation was combined with anti-PD-1 checkpoint blockade therapies, immune memory against glioblastoma was established, as demonstrated by treated mice that do not grow glioblastoma tumors after new glioblastoma inoculation. Immunohistochemistry and whole tumor cellular analysis demonstrated that nanoshell enhanced HIFU ablation converted an immune-suppressed “cold” tumor into an immune active “hot” tumor. An immunotherapy complementing acoustic therapeutic platform enabled by carefully designed ultrathin silica shells have been developed and can be highly relevant to the current rapid growth in use of immunotherapies against cancer.

Recommendations for Future Work

While a potential mechanism was proposed in figure 3.3a, additional cellular and cytokines can be measured to better elucidate a detailed mechanism. It has been suggested by other groups that tumor associated macrophage (TAM) polarization may affect tumor growth. Polarization to M1 macrophages are anti-tumor and would result in tumor growth suppression. In contrast, polarization to M2 macrophages are pro-tumor and may result in enhanced tumor proliferation and angiogenesis. Destructive therapeutic methods such as acoustic ablation, while minimizing thermal effects, may result in generation of wounds. As a result, it is very likely that TAM would be induced into M2 polarization, which suppresses immune responses, and promotes angiogenesis and connective tissue remodeling for wound healing and consequently, result in pro-tumor effects. Future work may involve the detailed cellular analysis of TAM polarization after acoustic ablation, in order to further fine tune acoustic ablation methods that maximizes M1/M2 ratios. Additional analysis on immune cell infiltrate dynamics may also provide in-depth answers on how anti-tumor immune cells can eventually penetrate the tumor after HIFU and aPD-1 combination treatments.

HIFU ablation in this work was done manually, relying on nanoshells to direct ablation regions. Nevertheless, it has been shown by other groups that the scanning pattern of ablation affects the degree of dendritic cell infiltration at the tumor. Smaller nanoparticles (<100 nm) that are more effective at accumulating at the tumor may better perfuse throughout the tumor for more uniform HIFU ablation. However, smaller silica nanoparticles were ineffective in HIFU ablation due to the decreased volume of encapsulated perfluocarbon liquid. Silica nanoshells with inner surface functionalized with long chain perfluorocarbons may act as perpetual cavitation sources and act as effective HIFU enhancement agents that are small.

REFERENCE

1. Chen F, Hong H, Zhang Y, Valdovinos HF, Shi S, Kwon GS, et al. In Vivo Tumor Targeting and Image-Guided Drug Delivery with Antibody-Conjugated, Radiolabeled Mesoporous Silica Nanoparticles. ACS Nano. 2013.

2. Fang W, Yang J, Gong J, Zheng N. Photo- and pH-Triggered Release of Anticancer Drugs from Mesoporous Silica-Coated Pd@Ag Nanoparticles. Advanced Funct Mater. 2012;22(4):842-8.

3. Giri S, Trewyn BG, Stellmaker MP, Lin VSY. Stimuli-Responsive Controlled-Release Delivery System Based on Mesoporous Silica Nanorods Capped with Magnetic Nanoparticles. Angew Chem Int Ed Engl. 2005;44(32):5038-44.

4. Kim HJ, Matsuda H, Zhou H, Honma I. Ultrasound-Triggered Smart Drug Release from a Poly(dimethylsiloxane)– Mesoporous Silica Composite. Adv Mater. 2006;18(23):3083-8.

5. Knežević NŽ, Trewyn BG, Lin VSY. Light- and pH-Responsive Release of Doxorubicin from a Mesoporous Silica-Based Nanocarrier. Chem Eur J. 2011;17(12):3338-42.

6. Kong SD, Zhang W, Lee JH, Brammer K, Lal R, Karin M, et al. Magnetically Vectored Nanocapsules for Tumor Penetration and Remotely Switchable On-Demand Drug Release. Nano Lett. 2010;10(12):5088-92.

7. Ortac I, Simberg D, Yeh Y-s, Yang J, Messmer B, Trogler WC, et al. Dual-porosity Hollow Nanoparticles for the Immunoprotection and Delivery of Non-human Enzymes. Nano Lett. 2014.

8. Slowing II, Trewyn BG, Lin VSY. Mesoporous Silica Nanoparticles for Intracellular Delivery of Membrane-Impermeable Proteins. J Am Chem Soc. 2007;129(28):8845-9.

9. Díaz JF, Balkus Jr KJ. Enzyme immobilization in MCM-41 molecular sieve. Journal of Molecular Catalysis B: Enzymatic. 1996;2(2–3):115-26.

10. Taylor KML, Kim JS, Rieter WJ, An H, Lin W, Lin W. Mesoporous Silica Nanospheres as Highly Efficient MRI Contrast Agents. J Am Chem Soc. 2008;130(7):2154-5.

11. Vivero-Escoto JL, Taylor-Pashow KML, Huxford RC, Della Rocca J, Okoruwa C, An H, et al. Multifunctional Mesoporous Silica Nanospheres with Cleavable Gd(III) Chelates as MRI Contrast Agents: Synthesis, Characterization, Target-Specificity, and Renal Clearance. Small. 2011;7(24):3519-28.

12. Hu H, Zhou H, Du J, Wang Z, An L, Yang H, et al. Biocompatiable hollow silica microspheres as novel ultrasound contrast agents for in vivo imaging. J Mater Chem. 2011;21(18):6576-83.

13. Santra S, Bagwe RP, Dutta D, Stanley JT, Walter GA, Tan W, et al. Synthesis and Characterization of Fluorescent, Radio-Opaque, and Paramagnetic Silica Nanoparticles for Multimodal Bioimaging Applications. Adv Mater. 2005;17(18):2165-9.

14. Nozawa K, Gailhanou H, Raison L, Panizza P, Ushiki H, Sellier E, et al. Smart Control of Monodisperse Stöber Silica Particles: Effect of Reactant Addition Rate on Growth Process. Langmuir. 2004;21(4):1516-23.

15. Cai Q, Lin W-Y, Xiao F-S, Pang W-Q, Chen X-H, Zou B-S. The preparation of highly ordered MCM-41 with extremely low surfactant concentration. Micropor Mesopor Mat. 1999;32(1–2):1-15.

16. Yang J, Lind JU, Trogler WC. Synthesis of Hollow Silica and Titania Nanospheres. Chem Mater. 2008;20(9):2875-7.

17. Caruso F, Caruso RA, Möhwald H. Nanoengineering of Inorganic and Hybrid Hollow Spheres by Colloidal Templating. Science. 1998;282(5391):1111-4.

18. Liu T, Li L, Teng X, Huang X, Liu H, Chen D, et al. Single and repeated dose toxicity of mesoporous hollow silica nanoparticles in intravenously exposed mice. Biomaterials. 2011;32(6):1657-68.

19. Xie G, Sun J, Zhong G, Shi L, Zhang D. Biodistribution and toxicity of intravenously administered silica nanoparticles in mice. Archives of toxicology. 2010;84(3):183-90.

20. Zhao Y, Trewyn BG, Slowing II, Lin VSY. Mesoporous Silica Nanoparticle-Based Double Drug Delivery System for Glucose-Responsive Controlled Release of Insulin and Cyclic AMP. J Am Chem Soc. 2009;131(24):8398-400.

21. Zhao D, Feng J, Huo Q, Melosh N, Fredrickson GH, Chmelka BF, et al. Triblock Copolymer Syntheses of Mesoporous Silica with Periodic 50 to 300 Angstrom Pores. Science. 1998;279(5350):548-52.

22. Tsai C-P, Chen C-Y, Hung Y, Chang F-H, Mou C-Y. Monoclonal antibody-functionalized mesoporous silica nanoparticles (MSN) for selective targeting breast cancer cells. J Mater Chem. 2009;19(32):5737-43.

23. Yokoi T, Yoshitake H, Tatsumi T. Synthesis of amino-functionalized MCM-41 via direct co-condensation and post-synthesis grafting methods using mono-, di- and tri-amino-organoalkoxysilanes. J Mater Chem. 2004;14(6):951-7.

24. Burleigh MC, Markowitz MA, Spector MS, Gaber BP. Direct Synthesis of Periodic Mesoporous Organosilicas: Functional Incorporation by Co-condensation with Organosilanes. The Journal of Physical Chemistry B. 2001;105(41):9935-42.

25. Huh S, Wiench JW, Yoo J-C, Pruski M, Lin VSY. Organic Functionalization and Morphology Control of Mesoporous Silicas via a Co-Condensation Synthesis Method. Chem Mater. 2003;15(22):4247-56.

26. Wang X, Chen H, Chen Y, Ma M, Zhang K, Li F, et al. Perfluorohexane-Encapsulated Mesoporous Silica Nanocapsules as Enhancement Agents for Highly Efficient High Intensity Focused Ultrasound (HIFU). Adv Mater. 2012;24(6):785-91.

27. Pohaku Mitchell KK, Liberman A, Kummel AC, Trogler WC. Iron(III)-Doped, Silica Nanoshells: A Biodegradable Form of Silica. Journal of the American Chemical Society. 2012;134(34):13997-4003.

28. Martinez HP, Kono Y, Blair SL, Sandoval S, Wang-Rodriguez J, Mattrey RF, et al. Hard shell gas-filled contrast enhancement particles for colour Doppler ultrasound imaging of tumors. Medchemcomm. 2010;1(4):266-70.

29. Zhang L, D'Acunzi M, Kappl M, Auernhammer GnK, Vollmer D, van Kats CM, et al. Hollow silica spheres: synthesis and mechanical properties. Langmuir. 2009;25(5):2711-7.

30. Voigt J-U. Ultrasound molecular imaging. Methods. 2009;48(2):92-7.

31. Sonne C, Xie F, Lof J, Oberdorfer J, Phillips P, Carr Everbach E, et al. Differences in definity and optison microbubble destruction rates at a similar mechanical index with different real-time perfusion systems. Journal of the American Society of Echocardiography. 2003;16(11):1178-85.

32. Liberman A, Martinez HP, Ta CN, Barback CV, Mattrey RF, Kono Y, et al. Hollow silica and silica-boron nano/microparticles for contrast-enhanced ultrasound to detect small tumors. Biomaterials. 2012;33(20):5124-9.

33. Liberman A, Wu Z, Barback CV, Viveros R, Blair SL, Ellies LG, et al. Color Doppler Ultrasound and Gamma Imaging of Intratumorally Injected 500 nm Iron–Silica Nanoshells. ACS Nano. 2013;7(7):6367-77.

34. Stride E, Saffari N. Microbubble ultrasound contrast agents: a review. Proceedings of the Institution of Mechanical Engineers, Part H: Journal of Engineering in Medicine. 2003;217(6):429-47.

35. Goldberg BB, Liu J-B, Forsberg F. Ultrasound contrast agents: a review. Ultrasound in medicine & biology. 1994;20(4):319-33.

36. Kerber RE, Kioschos JM, Lauer RM. Use of an ultrasonic contrast method in the diagnosis of valvular regurgitation and intracardiac shunts. The American journal of cardiology. 1974;34(6):722-7.

37. Cosgrove D. Ultrasound contrast agents: an overview. European journal of radiology. 2006;60(3):324-30.

38. De Jong N, Ten Cate F, Lancee C, Roelandt J, Bom N. Principles and recent developments in ultrasound contrast agents. Ultrasonics. 1991;29(4):324-30.

39. Forsberg F, Merton D, Liu J, Needleman L, Goldberg B. Clinical applications of ultrasound contrast agents. Ultrasonics. 1998;36(1):695-701.

40. Kiessling F, Fokong S, Koczera P, Lederle W, Lammers T. Ultrasound microbubbles for molecular diagnosis, therapy, and theranostics. Journal of nuclear medicine : official publication, Society of Nuclear Medicine. 2012;53(3):345-8.

41. Gramiak R, Shah PM. Echocardiography of the aortic root. Investigative radiology. 1968;3(5):356-66.

42. Gramiak R, Shah PM, Kramer DH. Ultrasound cardiography: contrast studies in anatomy and function. Radiology. 1969;92(5):939-48.

43. Bloch SH, Wan M, Dayton PA, Ferrara KW. Optical observation of lipid-and polymer-shelled ultrasound microbubble contrast agents. Applied Physics Letters. 2004;84(4):631-3.

44. Garg S, Thomas AA, Borden MA. The effect of lipid monolayer in-plane rigidity on< i> in vivo</i> microbubble circulation persistence. Biomaterials. 2013;34(28):6862-70.

45. Schutt EG, Klein DH, Mattrey RM, Riess JG. Injectable microbubbles as contrast agents for diagnostic ultrasound imaging: the key role of perfluorochemicals. Angewandte Chemie International Edition. 2003;42(28):3218-35.

46. Raisinghani A, DeMaria AN. Physical principles of microbubble ultrasound contrast agents. The American journal of cardiology. 2002;90(10):3-7.

47. Kabalnov A, Klein D, Pelura T, Schutt E, Weers J. Dissolution of multicomponent microbubbles in the bloodstream: 1. Theory. Ultrasound in medicine & biology. 1998;24(5):739-49.

48. Yasu T, Schmid-Schönbein GW, Cotter B, DeMaria AN. Flow dynamics of QW7437, a new dodecafluoropentane ultrasound contrast agent, in the microcirculation: microvascular mechanisms for persistent tissue echo enhancement. Journal of the American College of Cardiology. 1999;34(2):578-86.

49. Zeng J, See AP, Phallen J, Jackson CM, Belcaid Z, Ruzevick J, et al. Anti-PD-1 blockade and stereotactic radiation produce long-term survival in mice with intracranial gliomas. International Journal of Radiation Oncology* Biology* Physics. 2013;86(2):343-9.

50. Preusser M, Lim M, Hafler DA, Reardon DA, Sampson JH. Prospects of immune checkpoint modulators in the treatment of glioblastoma. Nature Reviews Neurology. 2015;11(9):504-14.

51. Ostrom QT, Gittleman H, Liao P, Rouse C, Chen Y, Dowling J, et al. CBTRUS Statistical Report: Primary Brain and Central Nervous System Tumors Diagnosed in the United States in 2007–2011. Neuro Oncol. 2014;16(suppl_4):iv1--iv63.

52. Curran MA, Montalvo W, Yagita H, Allison JP. PD-1 and CTLA-4 combination blockade expands infiltrating T cells and reduces regulatory T and myeloid cells within B16 melanoma tumors. Proceedings of the National Academy of Sciences. 2010;107(9):4275-80.

53. Duraiswamy J, Kaluza KM, Freeman GJ, Coukos G. Dual blockade of PD-1 and CTLA-4 combined with tumor vaccine effectively restores T cell rejection function in tumors. Cancer research. 2013:canres. 4100.2012.

54. Parry RV, Chemnitz JM, Frauwirth KA, Lanfranco AR, Braunstein I, Kobayashi SV, et al. CTLA-4 and PD-1 receptors inhibit T-cell activation by distinct mechanisms. Molecular and cellular biology. 2005;25(21):9543-53.

55. Hamid O, Robert C, Daud A, Hodi FS, Hwu W-J, Kefford R, et al. Safety and tumor responses with lambrolizumab (anti–PD-1) in melanoma. New England Journal of Medicine. 2013;369(2):134-44.

56. Topalian SL, Hodi FS, Brahmer JR, Gettinger SN, Smith DC, McDermott DF, et al. Safety, activity, and immune correlates of anti–PD-1 antibody in cancer. New England Journal of Medicine. 2012;366(26):2443-54.

57. Ferris RL, Blumenschein Jr G, Fayette J, Guigay J, Colevas AD, Licitra L, et al. Nivolumab for recurrent squamous-cell carcinoma of the head and neck. New England Journal of Medicine. 2016;375(19):1856-67.

58. Lim M, Xia Y, Bettegowda C, Weller M. Current state of immunotherapy for glioblastoma. Nature Reviews Clinical Oncology. 2018:1.

59. Filley AC, Henriquez M, Dey M. Recurrent glioma clinical trial, CheckMate-143: the game is not over yet. Oncotarget. 2017;8(53):91779-94.

60. Bell JC, Ilkow CS. A Viro-Immunotherapy Triple Play for the Treatment of Glioblastoma. Cancer Cell. 2017;32(2):133-4.

61. Lieberman NAP, DeGolier K, Kovar HM, Davis A, Hoglund V, Stevens J, et al. Characterization of the immune microenvironment of diffuse intrinsic pontine glioma: implications for development of immunotherapy. Neuro-Oncology. 2018:noy145-noy.

62. Ni K, Lan G, Chan C, Quigley B, Lu K, Aung T, et al. Nanoscale metal-organic frameworks enhance radiotherapy to potentiate checkpoint blockade immunotherapy. Nat Commun. 2018;9(1):2351.

63. Thariat J, Hannoun-Levi J-M, Sun Myint A, Vuong T, Gérard J-P. Past, present, and future of radiotherapy for the benefit of patients. Nat Rev Clin Oncol. 2012;10(1):52.

64. He C, Duan X, Guo N, Chan C, Poon C, Weichselbaum RR, et al. Core-shell nanoscale coordination polymers combine chemotherapy and photodynamic therapy to potentiate checkpoint blockade cancer immunotherapy. Nat Commun. 2016;7:12499.

65. Duan X, Chan C, Guo N, Han W, Weichselbaum RR, Lin W. Photodynamic Therapy Mediated by Nontoxic Core-Shell Nanoparticles Synergize with Immune Checkpoint Blockade to Elicit Antitumor Immunity and Antimetastatic Effect on Breast Cancer. Journal of the American Chemical Society. 2016.

66. Xu J, Xu L, Wang C, Yang R, Zhuang Q, Han X, et al. Near-Infrared-Triggered Photodynamic Therapy with Multitasking Upconversion Nanoparticles in Combination with Checkpoint Blockade for Immunotherapy of Colorectal Cancer. ACS Nano. 2017;11(5):4463--74.

67. Hu F, Zhang Y, Chen G, Li C, Wang Q. Double-Walled Au Nanocage/SiO2 Nanorattles: Integrating SERS Imaging, Drug Delivery and Photothermal Therapy. small. 2015;11(8):985-93.

68. Stolik S, Delgado JA, Pérez A, Anasagasti L. Measurement of the penetration depths of red and near infrared light in human “ex vivo” tissues. J Photochem Photobiol, B. 2000;57(2):90--3.

69. Hao X, Li C, Zhang Y, Wang H, Chen G, Wang M, et al. Programmable Chemotherapy and Immunotherapy against Breast Cancer Guided by Multiplexed Fluorescence Imaging in the Second Near-Infrared Window. Advanced Materials. 2018;30(51):1804437.

70. Zou W, Wolchok JD, Chen L. PD-L1 (B7-H1) and PD-1 pathway blockade for cancer therapy: Mechanisms, response biomarkers, and combinations. Science translational medicine. 2016;8(328):328rv4-rv4.

71. Orsi F, Zhang L, Arnone P, Orgera G, Bonomo G, Vigna PD, et al. High-intensity focused ultrasound ablation: effective and safe therapy for solid tumors in difficult locations. American journal of roentgenology. 2010;195(3):W245-W52.

72. Wu F, Wang Z-B, Cao Y-D, Chen W, Bai J, Zou J, et al. A randomised clinical trial of high-intensity focused ultrasound ablation for the treatment of patients with localised breast cancer. British journal of cancer. 2003;89(12):2227.

73. van den Bijgaart RJE, Eikelenboom DC, Hoogenboom M, Fütterer JJ, den Brok MH, Adema GJ. Thermal and mechanical high-intensity focused ultrasound: perspectives on tumor ablation, immune effects and combination strategies. Cancer Immunol Immunother. 2017;66(2):247--58.

74. Hoogenboom M, Eikelenboom D, den Brok MH, Veltien A, Wassink M, Wesseling P, et al. In vivo MR guided boiling histotripsy in a mouse tumor model evaluated by MRI and histopathology. NMR in Biomedicine. 2016;29(6):721-31.

75. Xing Y, Lu X, Pua EC, Zhong P. The effect of high intensity focused ultrasound treatment on metastases in a murine melanoma model. Biochem Biophys Res Commun. 2008;375(4):645--50.

76. Liberman A, Wu Z, Barback CV, Viveros RD, Wang J, Ellies LG, et al. Hollow iron-silica nanoshells for enhanced high intensity focused ultrasound. journal of surgical research. 2014;190(2):391-8.

77. Liberman A, Mendez N, Trogler WC, Kummel AC. Synthesis and surface functionalization of silica nanoparticles for nanomedicine. Surface Science Reports. 2014;69(2–3):132-58.

78. Mazur M. Electrochemically prepared silver nanoflakes and nanowires. Electrochemistry Communications. 2004;6(4):400-3.

79. Li S, Long B, Wang Z, Tian Y, Zheng Y, Zhang Q. Synthesis of hydrophobic zinc borate nanoflakes and its effect on flame retardant properties of polyethylene. Journal of Solid State Chemistry. 2010;183(4):957-62.

80. Reddy M, Yu T, Sow C-H, Shen ZX, Lim CT, Subba Rao G, et al. α-Fe2O3 Nanoflakes as an Anode Material for Li-Ion Batteries. Advanced Funct Mater. 2007;17(15):2792-9.

81. Hosono E, Fujihara S, Honma I, Ichihara M, Zhou H. Synthesis of the CoOOH fine nanoflake film with the high rate capacitance property. Journal of Power Sources. 2006;158(1):779-83.

82. Cui R, Lu W, Zhang L, Yue B, Shen S. Template-Free Synthesis and Self-Assembly of CeO2 Nanospheres Fabricated with Foursquare Nanoflakes. The Journal of Physical Chemistry C. 2009;113(52):21520-5.

83. Rognin NG, Frinking P, Costa M, Arditi M, editors. In-vivo perfusion quantification by contrast ultrasound: validation of the use of linearized video data vs. raw RF data. Ultrasonics Symposium, 2008 IUS 2008 IEEE; 2008: IEEE.

84. Voronkov MG, Mileshkevich VP, Yuzhelevskii YA. The siloxane bond. Consultants Bureau, New York. 1978:170.

85. Brochier Salon M-C, Bayle P-A, Abdelmouleh M, Boufi S, Belgacem MN. Kinetics of hydrolysis and self condensation reactions of silanes by NMR spectroscopy. Colloids and Surfaces A: Physicochemical and Engineering Aspects. 2008;312(2–3):83-91.

86. Brinker CJ, Scherer GW. Sol-gel science: the physics and chemistry of sol-gel processing: Academic press; 2013.

87. Pohaku Mitchell KK, Liberman A, Kummel AC, Trogler WC. Iron (III)-doped, silica nanoshells: a biodegradable form of silica. Journal of the American Chemical Society. 2012;134(34):13997-4003.

88. Liberman A, Mendez N, Trogler WC, Kummel AC. Synthesis and surface functionalization of silica nanoparticles for nanomedicine. Surface Science Reports. 2014;69(2-3):132-58.

89. Lo AH, Kripfgans OD, Carson PL, Rothman ED, Fowlkes JB. Acoustic droplet vaporization threshold: effects of pulse duration and contrast agent. Ultrasonics, Ferroelectrics and Frequency Control, IEEE Transactions on. 2007;54(5):933-46.

90. Kripfgans OD, Fowlkes JB, Miller DL, Eldevik OP, Carson PL. Acoustic droplet vaporization for therapeutic and diagnostic applications. Ultrasound in medicine & biology. 2000;26(7):1177-89.

91. Fabiilli ML, Haworth KJ, Fakhri NH, Kripfgans OD, Carson PL, Fowlkes JB. The role of inertial cavitation in acoustic droplet vaporization. Ultrasonics, Ferroelectrics and Frequency Control, IEEE Transactions on. 2009;56(5):1006-17.

92. Kripfgans OD, Fowlkes JB, Woydt M, Eldevik OP, Carson PL. In vivo droplet vaporization for occlusion therapy and phase aberration correction. Ultrasonics, Ferroelectrics and Frequency Control, IEEE Transactions on. 2002;49(6):726-38.

93. Zhang M, Fabiilli ML, Haworth KJ, Padilla F, Swanson SD, Kripfgans OD, et al. Acoustic droplet vaporization for enhancement of thermal ablation by high intensity focused ultrasound. Academic radiology. 2011;18(9):1123-32.

94. Wang X, Chen H, Chen Y, Ma M, Zhang K, Li F, et al. Perfluorohexane-Encapsulated Mesoporous Silica Nanocapsules as Enhancement Agents for Highly Efficient High Intensity Focused Ultrasound (HIFU). Advanced Materials. 2012;24(6):785-91.

95. Sheeran PS, Wong VP, Luois S, McFarland RJ, Ross WD, Feingold S, et al. Decafluorobutane as a phase-change contrast agent for low-energy extravascular ultrasonic imaging. Ultrasound in medicine & biology. 2011;37(9):1518-30.

96. Klibanov AL. Ligand-carrying gas-filled microbubbles: ultrasound contrast agents for targeted molecular imaging. Bioconjugate chemistry. 2005;16(1):9-17.

97. Qin S, Caskey CF, Ferrara KW. Ultrasound contrast microbubbles in imaging and therapy: physical principles and engineering. Physics in medicine and biology. 2009;54(6):R27.

98. Hashizume H, Baluk P, Morikawa S, McLean JW, Thurston G, Roberge S, et al. Openings between defective endothelial cells explain tumor vessel leakiness. The American journal of pathology. 2000;156(4):1363-80.

99. Danquah MK, Zhang XA, Mahato RI. Extravasation of polymeric nanomedicines across tumor vasculature. Advanced drug delivery reviews. 2011;63(8):623-39.

100. Nakamura Y, Mochida A, Choyke PL, Kobayashi H. Nanodrug Delivery: Is the Enhanced Permeability and Retention Effect Sufficient for Curing Cancer? Bioconjugate Chemistry. 2016;27(10):2225-38.

101. Yuan F, Dellian M, Fukumura D, Leunig M, Berk DA, Torchilin VP, et al. Vascular permeability in a human tumor xenograft: molecular size dependence and cutoff size. Cancer research. 1995;55(17):3752-6.

102. Hobbs SK, Monsky WL, Yuan F, Roberts WG, Griffith L, Torchilin VP, et al. Regulation of transport pathways in tumor vessels: role of tumor type and microenvironment. Proceedings of the National Academy of Sciences. 1998;95(8):4607-12.

103. Jain RK. Transport of molecules, particles, and cells in solid tumors. Annual review of biomedical engineering. 1999;1(1):241-63.

104. Jain RK, Stylianopoulos T. Delivering nanomedicine to solid tumors. Nature reviews Clinical oncology. 2010;7(11):653-64.

105. Moore A, Marecos E, Bogdanov Jr A, Weissleder R. Tumoral distribution of long-circulating dextran-coated iron oxide nanoparticles in a rodent model 1. Radiology. 2000;214(2):568-74.

106. Pinto JT, Suffoletto BP, Berzin TM, Qiao CH, Lin S, Tong WP, et al. Prostate-specific membrane antigen: a novel folate hydrolase in human prostatic carcinoma cells. Clinical Cancer Research. 1996;2(9):1445-51.

107. Ghosh A, Heston WD. Tumor target prostate specific membrane antigen (PSMA) and its regulation in prostate cancer. Journal of cellular biochemistry. 2004;91(3):528-39.

108. Hattori Y, Maitani Y. Enhanced in vitro DNA transfection efficiency by novel folate-linked nanoparticles in human prostate cancer and oral cancer. Journal of controlled release. 2004;97(1):173-83.

109. Xia W, Hilgenbrink AR, Matteson EL, Lockwood MB, Cheng J-X, Low PS. A functional folate receptor is induced during macrophage activation and can be used to target drugs to activated macrophages. Blood. 2009;113(2):438-46.

110. Hilgendorf I, Swirski FK. Folate Receptor: A Macrophage “Achilles' Heel”? Journal of the American Heart Association. 2012;1(4):e004036.

111. Wong CP, Bray TM, Ho E. Induction of proinflammatory response in prostate cancer epithelial cells by activated macrophages. Cancer letters. 2009;276(1):38-46.

112. Kamaly N, Xiao Z, Valencia PM, Radovic-Moreno AF, Farokhzad OC. Targeted polymeric therapeutic nanoparticles: design, development and clinical translation. Chemical Society Reviews. 2012;41(7):2971-3010.

113. Acharya S, Sahoo SK. PLGA nanoparticles containing various anticancer agents and tumour delivery by EPR effect. Advanced drug delivery reviews. 2011;63(3):170-83.

114. Weissleder R, Nahrendorf M, Pittet MJ. Imaging macrophages with nanoparticles. Nature materials. 2014;13(2):125-38.

115. Kumar R, Roy I, Ohulchanskky TY, Vathy LA, Bergey EJ, Sajjad M, et al. In vivo biodistribution and clearance studies using multimodal organically modified silica nanoparticles. ACS nano. 2010;4(2):699-708.

116. Godin B, Chiappini C, Srinivasan S, Alexander JF, Yokoi K, Ferrari M, et al. Discoidal porous silicon particles: fabrication and biodistribution in breast cancer bearing mice. Advanced functional materials. 2012;22(20):4225-35.

117. He X, Nie H, Wang K, Tan W, Wu X, Zhang P. In vivo study of biodistribution and urinary excretion of surface-modified silica nanoparticles. Analytical chemistry. 2008;80(24):9597-603.

118. Mendez N, Liberman A, Corbeil J, Barback C, Viveros R, Wang J, et al. Assessment of in vivo systemic toxicity and biodistribution of iron-doped silica nanoshells. Nanomedicine: Nanotechnology, Biology and Medicine. 2017;13(3):933-42.

119. Chen F, Hong H, Shi S, Goel S, Valdovinos HF, Hernandez R, et al. Engineering of hollow mesoporous silica nanoparticles for remarkably enhanced tumor active targeting efficacy. Scientific reports. 2014;4.

120. Willmann JK, van Bruggen N, Dinkelborg LM, Gambhir SS. Molecular imaging in drug development. Nature Reviews Drug Discovery. 2008;7(7):591-607.

121. Vivero-Escoto JL, Huxford-Phillips RC, Lin W. Silica-based nanoprobes for biomedical imaging and theranostic applications. Chemical Society Reviews. 2012;41(7):2673-85.

122. Liong M, Lu J, Kovochich M, Xia T, Ruehm SG, Nel AE, et al. Multifunctional inorganic nanoparticles for imaging, targeting, and drug delivery. ACS nano. 2008;2(5):889-96.

123. Stupp R, Mason WP, Van Den Bent MJ, Weller M, Fisher B, Taphoorn MJ, et al. Radiotherapy plus concomitant and adjuvant temozolomide for glioblastoma. New England Journal of Medicine. 2005;352(10):987-96.

124. Forsberg F, Merton DA, Liu JB, Needleman L, Goldberg BB. Clinical applications of ultrasound contrast agents. Ultrasonics. 1998;36(1):695-701.

125. Pirro V, Alfaro CM, Jarmusch AK, Hattab EM, Cohen-Gadol AA, Cooks RG. Intraoperative assessment of tumor margins during glioma resection by desorption electrospray ionization-mass spectrometry. Proceedings of the National Academy of Sciences. 2017;114(26):6700-5.

126. Iacob G, Dinca EB. Current data and strategy in glioblastoma multiforme. Journal of medicine and life. 2009;2(4):386.

127. Huang Z, Cheng L, Guryanova OA, Wu Q, Bao S. Cancer stem cells in glioblastoma—molecular signaling and therapeutic targeting. Protein & cell. 2010;1(7):638-55.

128. Lara-Velazquez M, Al-Kharboosh R, Jeanneret S, Vazquez-Ramos C, Mahato D, Tavanaiepour D, et al. Advances in brain tumor surgery for glioblastoma in adults. Brain sciences. 2017;7(12):166.

129. Selbekk T, Jakola AS, Solheim O, Johansen TF, Lindseth F, Reinertsen I, et al. Ultrasound imaging in neurosurgery: approaches to minimize surgically induced image artefacts for improved resection control. Acta neurochirurgica. 2013;155(6):973-80.

130. Liberman A, Wang J, Lu N, Viveros RD, Allen C, Mattrey R, et al. Mechanically Tunable Hollow Silica Ultrathin Nanoshells for Ultrasound Contrast Agents. Advanced Functional Materials. 2015.

131. Ching-Hsin Huang JW, Jian Yang, Juan Pablo Oviedo, Seungjin Nam, William C. Trogler, Sarah L. Blair, Moon J. Kim, Andrew C. Kummel. Thickness and Sphericity Control of 2 μm Silica Shells Through Iron Doping: Low Threshold Hard Shell Ultrasound Contrast Agents. Advanced Materials. 2019;In Preparation.

132. Fabiilli ML, Haworth KJ, Fakhri NH, Kripfgans OD, Carson PL, Fowlkes JB. The role of inertial cavitation in acoustic droplet vaporization. IEEE transactions on ultrasonics, ferroelectrics, and frequency control. 2009;56(5).

133. Shpak O, Verweij M, Vos HJ, de Jong N, Lohse D, Versluis M. Acoustic droplet vaporization is initiated by superharmonic focusing. Proceedings of the National Academy of Sciences. 2014;111(5):1697-702.

134. Chen H, Li X, Wan M. Spatial–temporal dynamics of cavitation bubble clouds in 1.2 MHz focused ultrasound field. Ultrasonics sonochemistry. 2006;13(6):480-6.

135. Maloney E, Hwang JH. Emerging HIFU applications in cancer therapy. International Journal of Hyperthermia. 2015;31(3):302-9.

136. MacDonell J, Patel N, Rubino S, Ghoshal G, Fischer G, Burdette EC, et al. Magnetic resonance–guided interstitial high-intensity focused ultrasound for brain tumor ablation. Neurosurgical focus. 2018;44(2):E11.

137. Randomized Comparisons of Radiotherapy and Nitrosoureas for the Treatment of Malignant Glioma after Surgery | NEJM. 1980. p. 1323--9.

138. Nawaz S, Heindl A, Koelble K, Yuan Y. Beyond immune density: critical role of spatial heterogeneity in estrogen receptor-negative breast cancer. Modern Pathology. 2015;28(6):766.

139. Chetty R, Gatter K. CD3: structure, function, and role of immunostaining in clinical practice. The Journal of pathology. 1994;173(4):303-7.

140. Zhang M, Kleber S, Röhrich M, Timke C, Han N, Tuettenberg J, et al. Blockade of TGF-β Signaling by the TGFβR-I Kinase Inhibitor LY2109761 Enhances Radiation Response and Prolongs Survival in Glioblastoma. Cancer Research. 2011;71(23):7155-67.

141. Ma Y, Cheng Z, Liu J, Torre-Healy L, Lathia JD, Nakano I, et al. Inhibition of Farnesyltransferase Potentiates NOTCH-Targeted Therapy against Glioblastoma Stem Cells. Stem Cell Reports. 2017;9(6):1948-60.

142. Velpula KK, Bhasin A, Asuthkar S, Tsung AJ. Combined targeting of PDK1 and EGFR triggers regression of glioblastoma by reversing the Warburg effect. Cancer research. 2013;73(24):7277-89.

143. Zhan C, Gu B, Xie C, Li J, Liu Y, Lu W. Cyclic RGD conjugated poly (ethylene glycol)-co-poly (lactic acid) micelle enhances paclitaxel anti-glioblastoma effect. Journal of Controlled Release. 2010;143(1):136-42.

144. Altin JG, Sloan EK. The role of CD45 and CD45-associated molecules in T cell activation. Immunology and cell biology. 1997;75(5):430.

145. Eerola A-K, Soini Y, Pääkkö P. A High Number of Tumor-infiltrating Lymphocytes Are Associated with a Small Tumor Size, Low Tumor Stage, and a Favorable Prognosis in Operated Small Cell Lung Carcinoma. Clinical Cancer Research. 2000;6(5):1875-81.

146. Watanabe Y, Kuribayashi K, Miyatake S, Nishihara K, Nakayama E, Taniyama T, et al. Exogenous expression of mouse interferon gamma cDNA in mouse neuroblastoma C1300 cells results in reduced tumorigenicity by augmented anti-tumor immunity. Proceedings of the National Academy of Sciences. 1989;86(23):9456-60.

147. Dostert C, Pétrilli V, Van Bruggen R, Steele C, Mossman BT, Tschopp J. Innate Immune Activation Through Nalp3 Inflammasome Sensing of Asbestos and Silica. Science. 2008;320(5876):674-7.

148. Ghiringhelli F, Apetoh L, Tesniere A, Aymeric L, Ma Y, Ortiz C, et al. Activation of the NLRP3 inflammasome in dendritic cells induces IL-1β–dependent adaptive immunity against tumors. Nature Medicine. 2009;15:1170.

149. Deng J, Zhang Y, Feng J, Wu F. Dendritic Cells Loaded with Ultrasound-Ablated Tumour Induce in vivo Specific Antitumour Immune Responses. Ultrasound Med Biol. 2010;36(3):441--8.

150. Jolesz F, Clement GT, McDannold N, Black P, Hynynen K. Transcranial Magnetic Resonance Imaging– Guided Focused Ultrasound Surgery of Brain Tumors: Initial Findings in 3 Patients. Neurosurgery. 2010;66(2):323-32.